Global analysis of the selected turbine for the OWC

DATE: April 2018

PROJECT COORDINATOR:

WavEC Offshore Renewables

GRANT AGREEMENT NR: 641334

PROJECT: WETFEET

The WETFEET – Wave Energy Transition to Future by Evolution of Engineering and Technology project has received funding from the European Union's Horizon 2020 programme under grant agreement No 641334.

Report with global analysis of the selected turbine for the OWC based on the bench tests and further engineering considerations			
Project	WETFEET – Wave Energy Transition to Future by Evolution of Engineering and Technology		
WP No.	4	WP Title	Electro-mechanic PTO Breakthrough
Deliverable No.		4.3	
Nature (R: *Report*, P: *Prototype*, O: *Other*)		R	
Dissemination level (PU, PP, RE, CO)		PU	
Lead beneficiary:		IST	
Contributing partners			
Authors List:		L. M. C. Gato, B. S. Lopes, D. N. Ferreira, A. A. D. Carrelhas, A. F. O. Falcão, J. C. C. Henriques	
Quality reviewer		Peter Fraenkel	
Status (F: final; D: draft; RD: revised draft):		F	
Due Delivery Date:		31-10-2017	
Actual Delivery Date:		25-04-2018	

Version no.	Dates and comments
1	03-04-2018 First draft
2	13-04-2018 Quality review received
3	25-04-2018 Final version

Table of Contents

Table of figures

Table of tables

1. Introduction

The report presents the global analysis of the selected power-take-off system (PTO) for the oscillating water column (OWC) wave energy converter (WEC) based on the bench tests and presents further engineering considerations on the turbine design.

The selected PTO for the OWC WEC is the self-rectifying twin-rotor air turbine. The turbine (see Figure 1-2) is based on a pair of conventional radial-inflow rotors mounted on a common shaft, complemented by the corresponding inlet guide vane rows, by a curved-duct manifold arranged circumferentially in a periodic manner and by a two-position axially-moving cylindrical valve. The valve ensures that the air flows alternately through one or the other of the two parts of the twin-rotor turbine, depending on the sign of the pressure head. For this reason, only one half of the turbine was constructed.

The experimental tests were performed at the blow-down test rig of the Instituto Superior Técnico Turbomachinery Laboratory.

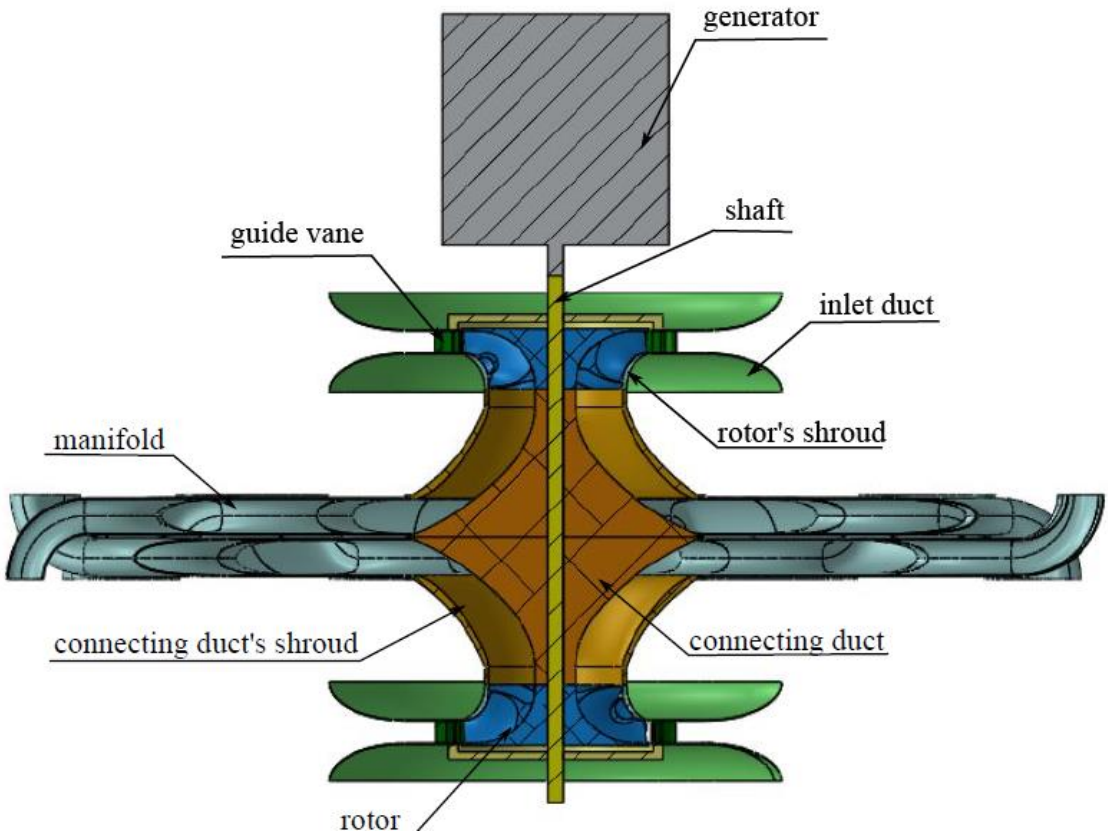

FIGURE 1. SCHEMATIC VIEW OF THE SELF-RECTIFYING TWIN-ROTOR RADIAL FLOW AIR TURBINE.

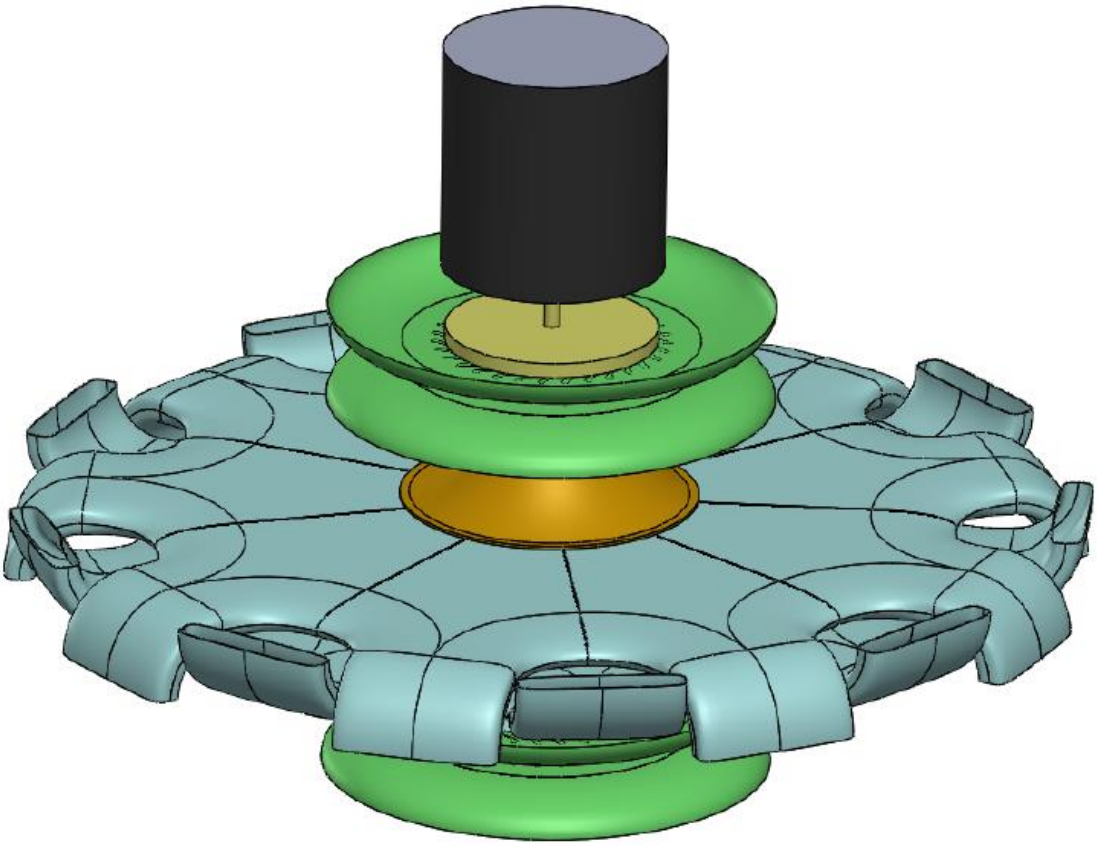

FIGURE 2. ISOMETRIC VIEW OF THE SELF-RECTIFYING TWIN-ROTOR RADIAL FLOW AIR TURBINE.

Section 2 describes the experimental apparatus and the instrumentation. The results are presented in section 3. Section 4 presents the engineering considerations. Finally, section 5 deals with the conclusions.

2. Test rig

2.1. Experimental apparatus

The layout of the test rig is presented in Figure 3. Air is sucked through the inlet duct into the turbine directly from the atmosphere. The air is discharged from the curved-duct manifold directly to the plenum chamber of the test rig. The plenum chamber contains a honeycomb lattice, whose function is to remove any swirl before the air enters into a calibrated nozzle, downstream of which there is a radial-flow fan driven by a controlled electrical motor. The turbine rotor was coupled to an electrical motor/generator whose rotational speed could be controlled. The air flow was assumed incompressible throughout the experiments. The pressure head across the turbine was provided by a conventional radial-flow fan driven by a 160 kW electrical motor whose rotational speed could be controlled. The turbine shaft was connected to a Datum Electronics M425 Torque Transducer which gave the torque and the rotational speed. Special attention was taken to avoid air leaks in the circuit. Figure 4 presents a photograph of the test rig.

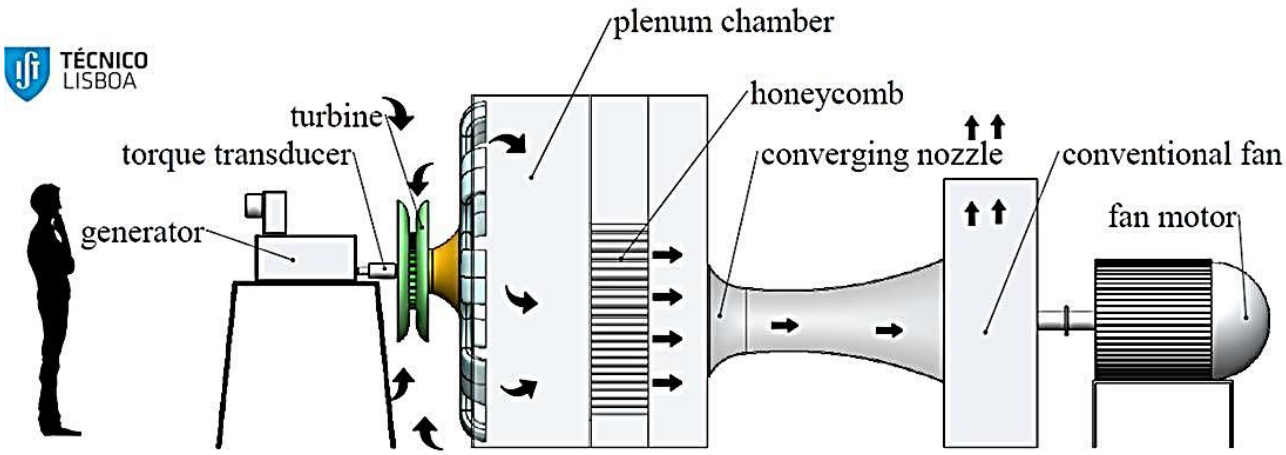

FIGURE 3. LAYOUT OF THE TEST RIG.

FIGURE 4. LAYOUT OF THE TEST RIG, SHOWING THE ELECTRICAL MOTOR/GENERATOR, THE INLET DUCT AND THE MANIFOLD.

2.2. Instrumentation

In order to evaluate the turbine performance, measurements were undertaken of volumetric flow rate, torque, rotational speed, temperature, humidity, atmospheric pressure and static pressure.

2.2.1. Volumetric flow rate

The volumetric flow rate is an important parameter to evaluate the overall performance of a turbine. It was decided to measure the volumetric flow at the inlet to the guide vane system, at a radial distance of 77 mm upstream of the inlet guide vanes, from the static pressure relative

to the atmosphere (see point 1 in Figure 12). At the inlet of the guide vanes, the flow is approximately uniform and it is possible to measure the volumetric flow rate with good accuracy.

The relation between the static pressure and the volumetric flow rate was obtained by calibration. In order to obtain that relation, traverses at the inlet were performed for different volumetric flow rates. Traverses were performed axially, between the walls of the inlet ducts. Figure 5 presents the velocity, U, along with the dimensionless axial coordinate, z^*. The volumetric flow rate was obtained by integration of the velocity profile.

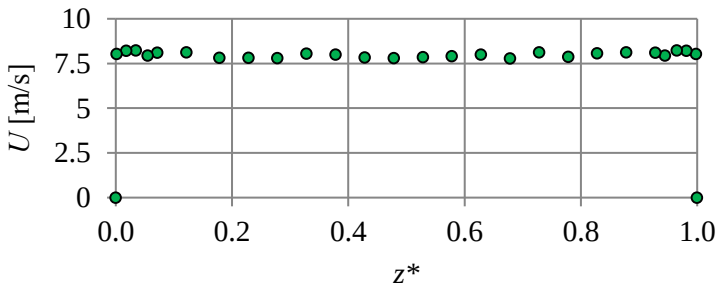

FIGURE 5. INLET TRAVERSE TO $Q = 1.194\ \mathrm{m}^3/s$.

This procedure was repeated for nine values of the volumetric flow rate. All the measured points are plotted in Figure 6. The same figure shows the parabolic curve that establishes the relationship between the static pressure and the volumetric flow rate.

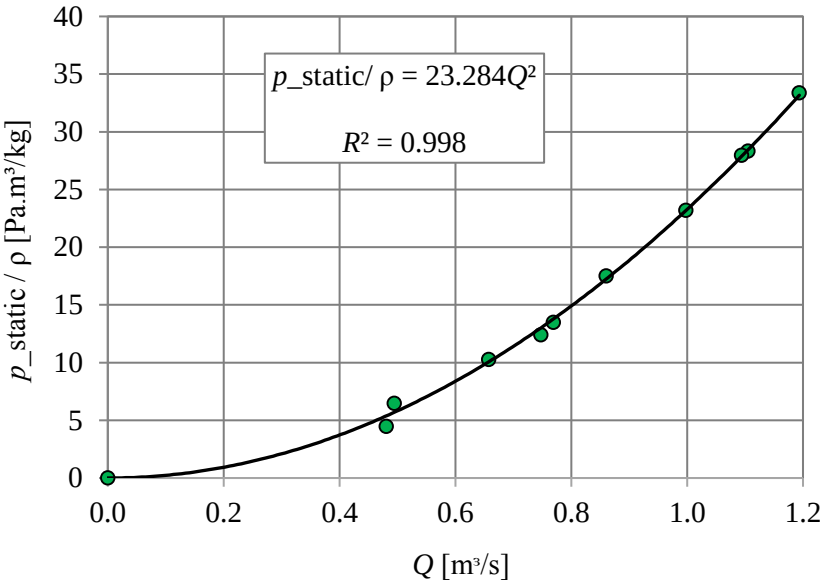

FIGURE 6. RELATION BETWEEN THE STATIC PRESSURE AND THE VOLUMETRIC FLOW RATE.

2.2.2. Torque and rotational speed

As mentioned before, the turbine shaft was connected to a torque transducer which gave the torque and the rotational speed. The torque transducer was selected based on the expected torque range to be observed during the measurements.

Two Datum Electronics M425 sensors were used during the measurements, with the ranges 0-10 Nm (see Figure 7) and 0-50 Nm (see Figure 8).

FIGURE 7. TORQUE TRANSDUCER: RANGE 0-10 NM.

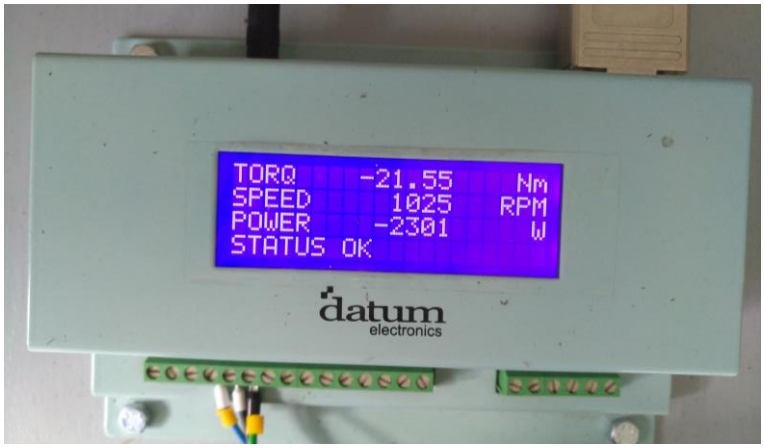

FIGURE 8. DATUM TORQUE TRANSDUCER MONITOR SHOWING TORQUE, SPEED AND POWER.

2.2.3. Temperature, humidity and atmospheric pressure

Air density depends on the temperature, humidity and the atmospheric pressure. The temperature was measured using an LM35-TO92 precision temperature sensor from National Instruments, Figure 9. The sensor has an output voltage linearly-proportional to the temperature:

$$V_{\text{out}} = 10\ \text{mV/°C} \times T, \qquad (2.1)$$

where V_{out} is the LM35-TO92 output voltage and T is the temperature in °C.

FIGURE 9. LM35-TO92 PRECISION TEMPERATURE SENSOR.

Humidity was measured using an adequate sensor HIH-4000-001 from Honeywell, Figure 10. This sensor accounts for the supply voltage and the room temperature:

$$V_{\text{out}} = V_{\text{supply}}(0.0062(\text{sensor RH}) + 0.16), \qquad (2.2)$$

$$\text{True RH} = \frac{\text{sensor RH}}{1.0546 - 0.00216T}, \tag{2.3}$$

where V_{out} is the output voltage, V_{supply} is the supply voltage, (sensor RH) is the humidity measured by the sensor, T is the room temperature in °C and True RH is the humidity compensated with the room temperature.

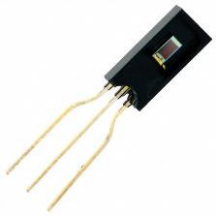

FIGURE 10. HIH-4000-001 HUMIDITY SENSOR.

The atmospheric pressure was measured using a Testo 511 – Absolute Pressure Meter, Figure 11.

FIGURE 11. TESTO 511 PRESSURE SENSOR.

2.2.4. Static pressure

The five static pressure stations are represented in Figure 12:

1) At the inlet duct;
2) Between the guide vanes and the rotor;
3) At the rotor exit;
4) At the diffuser inlet;
5) In the plenum chamber.

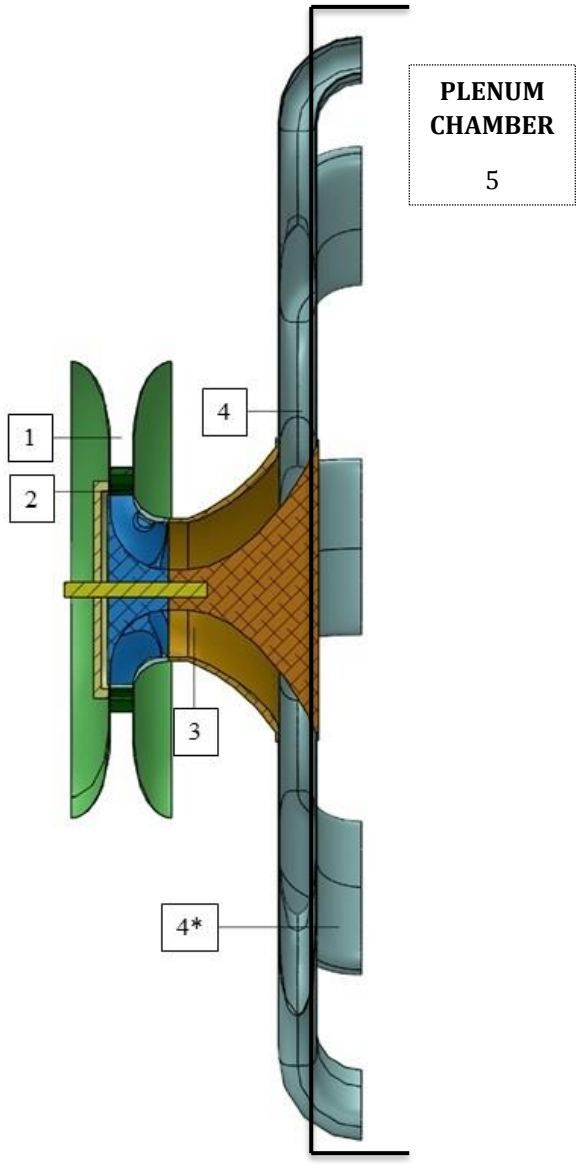

FIGURE 12. STATIC PRESSURE STATIONS.

Differential pressure transducers were used to measure the pressure in each station. The adequate pressure sensor was selected based on the expected pressure range for each section. All pressure sensors were calibrated using one Betz manometer.

Eight differential pressure transducers with different ranges (see Figure 13Figure 14) were used during the experimental tests, Table 1.

Manometer	Pressure range
1MBAR-D4V [1]	0-10 mmH_2O
1MBAR-D4V [2]	0-10 mmH_2O
FC9112113	0-19.9 mmH_2O (scale 10%) 0-199.9 mmH_2O (scale 100%)
FC91122114	0-19.9 mmH_2O (scale 10%) 0-199.9 mmH_2O (scale 100%)
FC9610126	0-1.9 mmH_2O (scale 10%) 0-19.9 mmH_2O (scale 100%)
GE1	0-102 mmH_2O
GE2	0-76 mmH_2O
GE3	0-204 mmH_2O

TABLE 1. PRESSURE TRANSDUCERS RANGE.

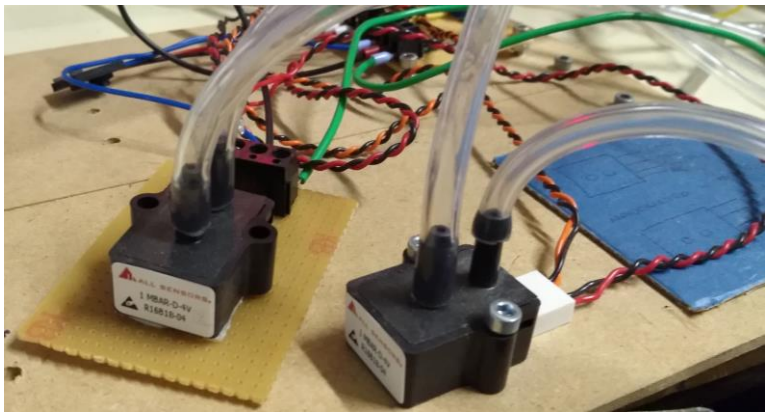

FIGURE 13. MANOMETERS 1MBAR-D4V [1] AND 1MBAR-D4V [2].

FIGURE 14. MANOMETER FC9610126, SCALE 100%.

FIGURE 15. MANOMETERS GE1, GE2 AND GE3.

2.2.5. Three-hole probe

The three-hole probe is an instrument used to measure the velocity pressure and the yaw angle of the flow velocity vector. The probe has three measuring holes: a central hole and two lateral ones. The velocity is determined using the measured pressure in each hole. This instrument was used during traverses at rotor inlet, at the rotor exit and in the diffuser (see Figure 16).

The three-hole probe was calibrated at the wind tunnel of the Instituto Superior Técnico Aerodynamic Laboratory, Figure 17.

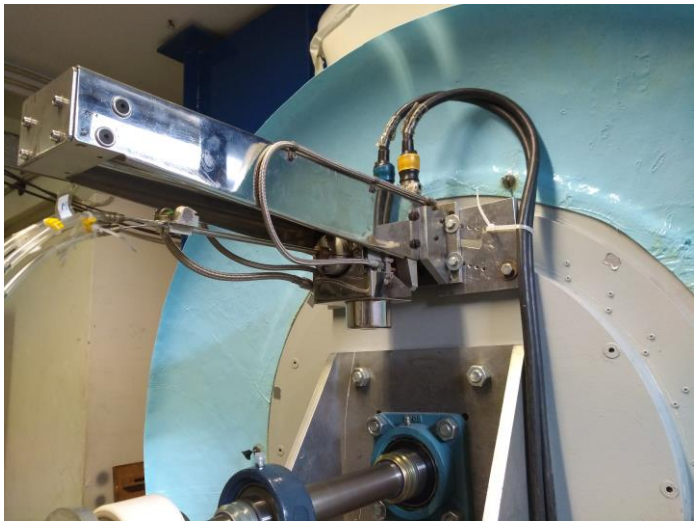

FIGURE 16. ROTOR INLET TRAVERSES USING THE THREE-HOLE PROBE.

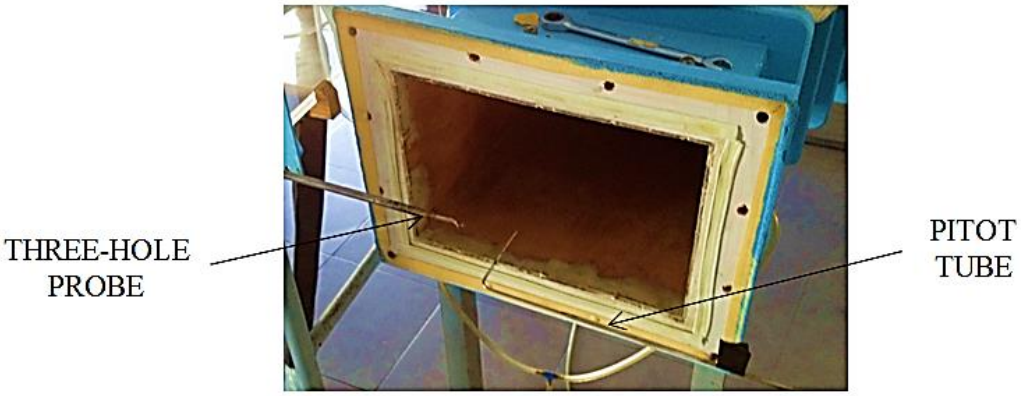

FIGURE 17. THREE-HOLE PROBE CALIBRATION.

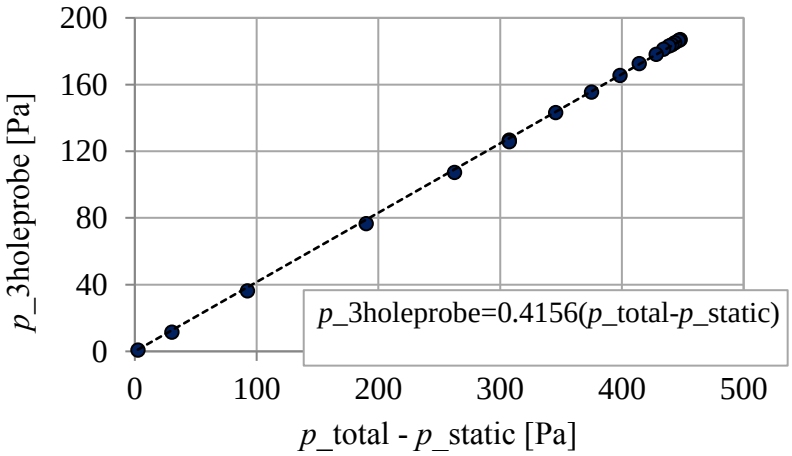

FIGURE 18. CALIBRATION OF THE THREE-HOLE PROBE.

The objective of the calibration is to find the relation between the pressure measured by the three-hole probe and a pressure measured by a Pitot tube relative to the atmosphere (p_total - p_static). The calibration results are plotted in Figure 18.

According to the previous results the calibration constant of the three-hole probe is 0.4156.

2.2.6. Data acquisition system

The data acquisition system was composed by a sensor (or more), a data acquisition board and a computer, see Figure 19.

FIGURE 19. DATA ACQUISITION SYSTEM.

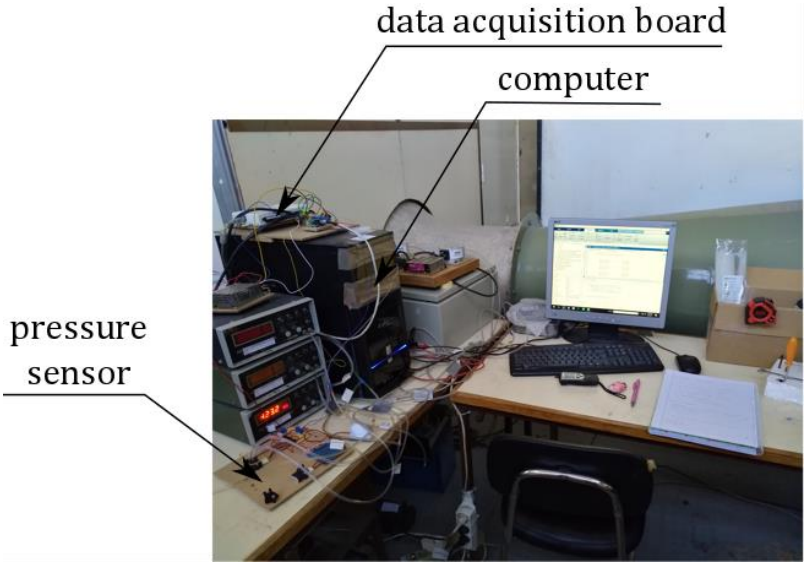

FIGURE 20. DATA ACQUISITION SYSTEM AT TURBOMACHINERY LABORATORY.

Each sensor converts a physical quantity into a measurable electric signal. The data acquisition board acts as the interface between the sensor and the computer. Finally, the computer is used to process, visualize and save the measurements.

The data acquisition board used during all the measurements was National Instruments 6221 M series, see Figure 20. All the instruments were calibrated in order to convert the sensor voltage to the proper unit (e.g. convert voltage into pressure).

3. Results

The use of dimensionless variables has the advantage of extending the applicability of the results from the testing of a given machine to geometrically similar machines of different sizes, at various rotational speeds and with different fluid densities. We introduce the following dimensionless variables:

$$\Phi = \frac{\mathrm{Q}}{\Omega \mathrm{D}^3}, \qquad \Psi = \frac{\Delta p}{\rho \Omega^2 \mathrm{D}^2}, \qquad \Pi = \frac{\mathrm{T}}{\rho \Omega^2 \mathrm{D}^5}, \qquad \eta_{ts} = \frac{\Pi}{\Phi \Psi}, \tag{3.1}$$

here Δp is pressure head, D is turbine diameter, Q is volumetric flow rate, T is turbine torque, ρ is air density, Ω is rotational speed (in radians per unit time), Φ is dimensionless flow rate, Ψ is dimensionless pressure head, Π is dimensionless power output and η_{ts} is total-to-static efficiency.

3.1. Friction torque for zero flow rate

The friction torque (for zero flow rate) has two components: aerodynamic and bearing losses. It is important to separately determine these components. The bearing torque losses are expected to be approximately independent of the rotational speed, while the aerodynamic losses or windage losses (for zero flow rate and large enough rotational speed) are expected to be proportional to the square of the rotational speed. Consequently, we expect the measured friction torque to be of the form

$$T_{\mathrm{friction}} = a + b\Omega^2. \tag{3.2}$$

The variation of friction losses with the rotational speed is represented in Figure 21. Interpolating the results by a polynomial with zero and second order terms, we can determine both components

$$T_{\mathrm{friction}} = 0.7836 + 6.6585 \times 10^{-5}\Omega^2. \tag{3.3}$$

The constant term represents the bearing torque whereas the second-order term represents the aerodynamic loss torque (windage loss).

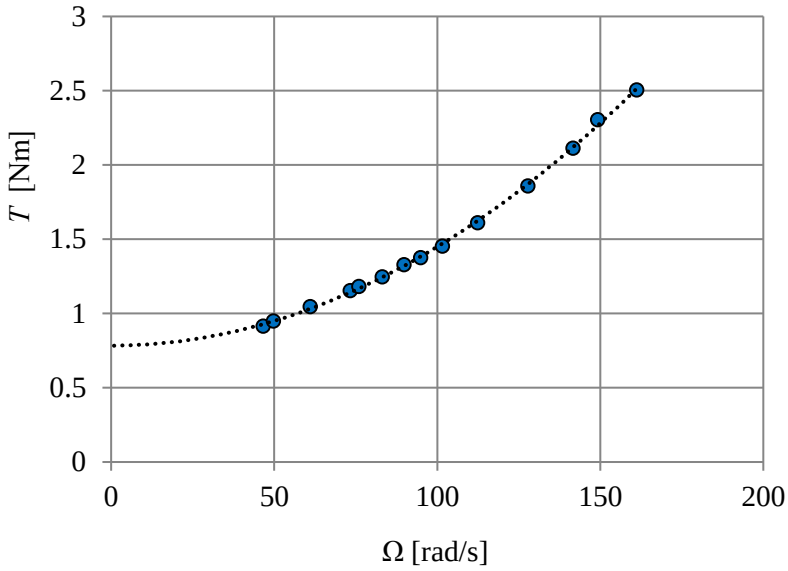

FIGURE 21. FRICTION TORQUE VERSUS ROTATIONAL SPEED.

In order to confirm the determined constants, two more tests were performed. In the first test, the decay of the rotational speed with the time was recorded. The results are plotted in Figure 22. In the second one, the torque variation with the volumetric flow rate was evaluated, Figure 23. Extrapolating the results for zero flow rate we can determine the bearing losses.

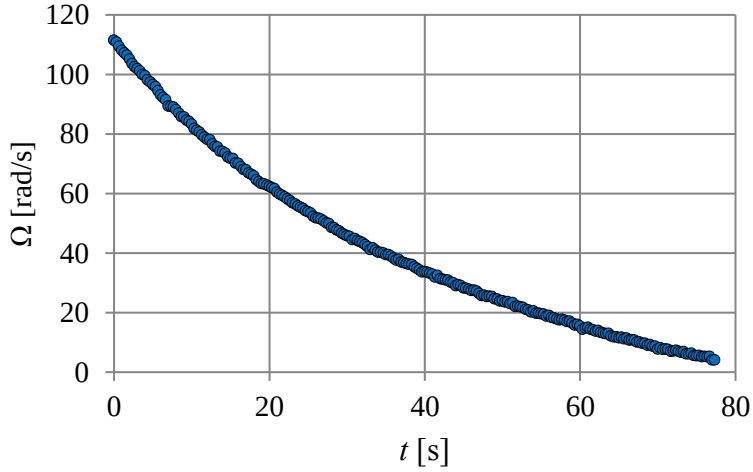

FIGURE 22. ROTATIONAL SPEED DECAY ALONG THE TIME.

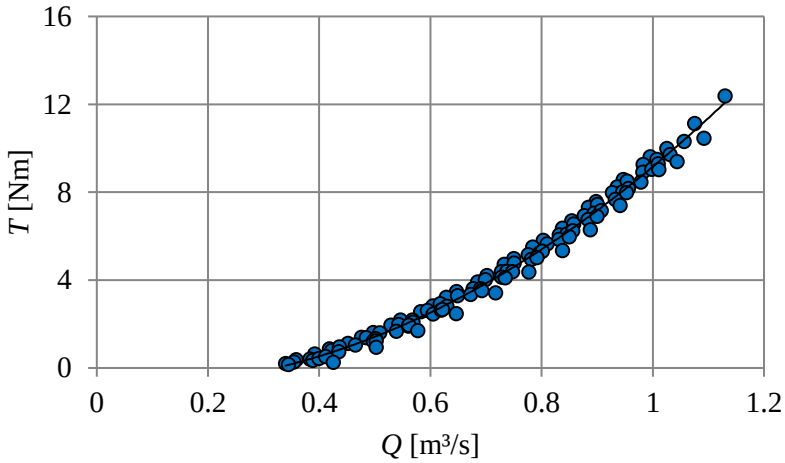

FIGURE 23. TORQUE VARIATION WITH VOLUMETRIC FLOW RATE.

The torque absorbed in bearings was added to the measured torque because it depends on the installation and should not be regarded as an intrinsic characteristic of the turbine. The twin-rotor turbine has two radial-inflow rotors mounted on a common shaft, as explained before. Both rotors are rotating at the same rotational speed but there is flow in only one. The passive rotor (the one without flow) is absorbing part of the energy. The amount of absorbed energy is dependent on rotational speed and corresponds to the aerodynamic losses (windage loss) determined previously. In the study of the performance of the twin-rotor turbine, the windage loss was subtracted from the measured power output of the turbine.

3.2. Rotor traverses

Detailed traverses were performed at rotor entrance and exit using a three-hole probe for four dimensionless flow rate coefficients: $\Phi_1 = 0.040$, $\Phi_2 = 0.050$, $\Phi_3 = 0.058$ and $\Phi_4 = 0.070$. It is important to have identical experimental conditions in the different traverses in order to analyse the results along the turbine. However, this was difficult, because ambient conditions cannot be controlled and the rotational speed was controlled manually. The rotational speed during the traverses was maintained at 111 ± 1.57 rad/s.

Detailed traverses at rotor entrance were performed in the axial direction at 7 equally spaced circumferential stations so as to cover a complete angular pitch of the inlet guide vane row $360/31 = 11.6°$. The angle between two consecutive positions was $2°$. We define the normalized angle in the circumferential direction as $\theta^* = \theta/11.6°$. Figure 24Figure 24 shows the

variation of the mean flow angle with the circumferential direction for the different flow rates. The mean flow angle, $\bar{\alpha}_2$, is defined as

$$\bar{\alpha}_2 = \frac{\arctan\left(V_{2\theta}/V_{2\mathrm{m}}\right)}{\arctan\left(\bar{V}_{2\theta}/\bar{V}_{2m}\right)}, \tag{3.4}$$

where $\bar{V}_{2\theta}$ and $\bar{V}_{2\mathrm{m}}$ are, respectively, the mean meridional and the mean circumferential components of the velocity defined as

$$\bar{V}_{2\theta} = Z \frac{\int_{z_1}^{z_2}\int_{\theta_0}^{\theta_{\mathrm{pitch}}} V_{2\theta} R_{2*} \mathrm{d}\theta\, \mathrm{d}z}{\int_{z_1}^{z_2}\int_{0}^{2\pi} R_{2*} \mathrm{d}\theta\, \mathrm{d}z}, \tag{3.5}$$

$$\bar{V}_{2m} = Z \frac{\int_{z_1}^{z_2}\int_{\theta_0}^{\theta_{\mathrm{pitch}}} V_{2m} R_{2*} \mathrm{d}\theta\, \mathrm{d}z}{\int_{z_1}^{z_2}\int_{0}^{2\pi} R_{2*} \mathrm{d}\theta\, \mathrm{d}z}. \tag{3.6}$$

Here z is axial direction, θ is circumferential direction and Z is the number of rotor blades. Traverses were performed at radius $R_{2*} = 0.257\mathrm{m}$.

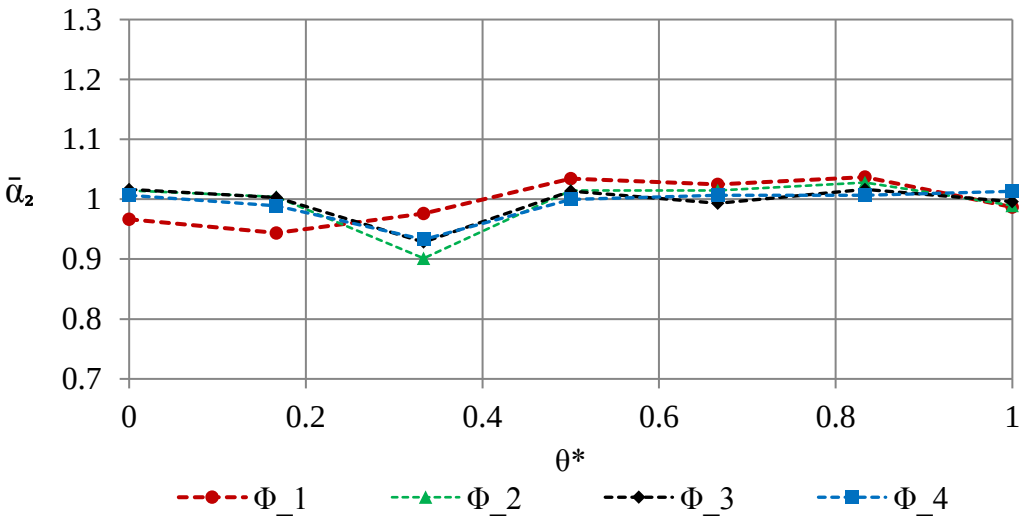

FIGURE 24. DIMENSIONLESS PLOT OF THE VELOCITY ANGLE ALONG THE CIRCUMFERENTIAL DIRECTION AT ROTOR ENTRANCE.

Figure 25 shows that the mean angle depends on the circumferential coordinate but is almost independent of the volumetric flow rate. The determined mean angles, for the different circumferential coordinates, are very close to the design angle ($\alpha_2 = 74°$).

Figure 26 presents the dimensionless velocity components $V^*_{2\mathrm{m}} = V_{2\mathrm{m}}/\bar{V}_{2\mathrm{m}}$ and $V^*_{2\theta} = V_{2\theta}/\bar{V}_{2\mathrm{m}}$ along the circumferential direction. Velocity components $V_{2\mathrm{m}}$ and $V_{2\theta}$ are defined as

$$V_{2\mathrm{m}} = \frac{\int_{\theta_1}^{\theta_2}\int_{z_1}^{z_2} V_{2\mathrm{m}}(b)R_{2*}\mathrm{d}z\,\mathrm{d}\theta}{\int_{\theta_1}^{\theta_2}\int_{z_1}^{z_2} R_{2*}\mathrm{d}z\,\mathrm{d}\theta}, \tag{3.7}$$

$$V_{2\theta} = \frac{\int_{\theta_1}^{\theta_2}\int_{z_1}^{z_2} V_{2\mathrm{m}}(b)V_{2\theta}(b)R_{2*}\mathrm{d}z\,\mathrm{d}\theta}{\int_{\theta_1}^{\theta_2}\int_{z_1}^{z_2} V_{2\mathrm{m}}(b)R_{2*}\mathrm{d}z\,\mathrm{d}\theta}. \tag{3.8}$$

Figure 26 shows that the meridional velocity component, $V^*_{2\mathrm{m}}$, is nearly independent of the volumetric flow rate and of the circumferential direction. Differently, the circumferential component, $V^*_{2\theta}$, varies with the circumferential coordinate and in some cases also with the volumetric flow rate. There is a negative peak in the circumferential component at $\theta^* = 1/3$.

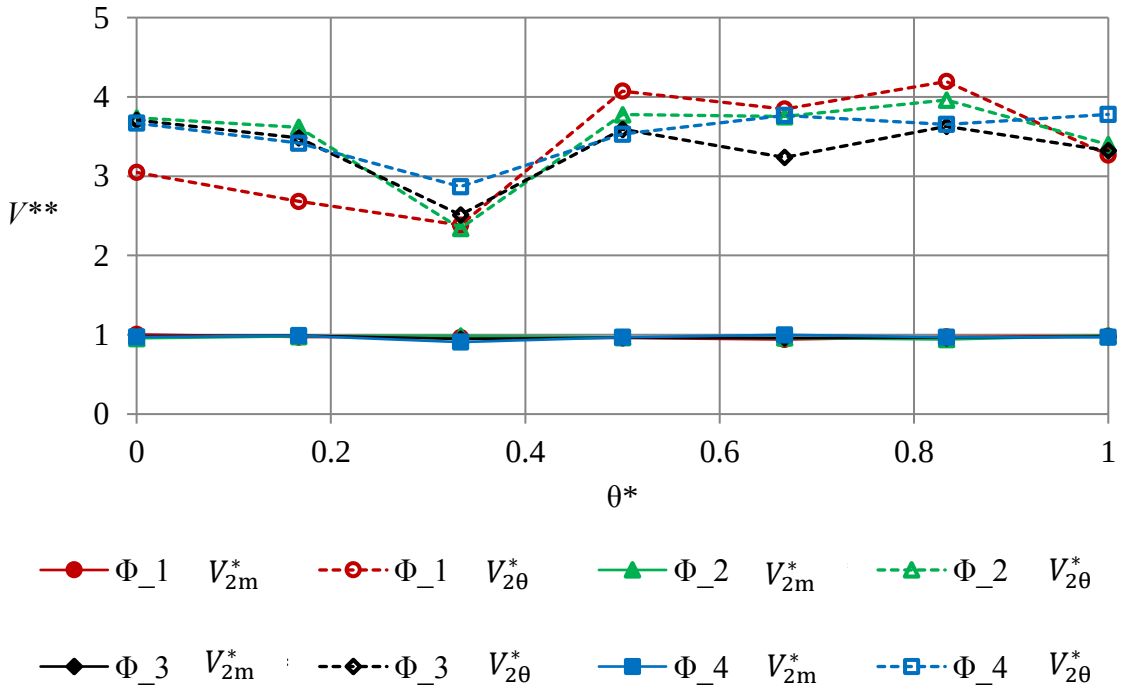

FIGURE 25. DIMENSIONLESS VELOCITY COMPONENTS ALONG THE CIRCUMFERENTIAL DIRECTION FOR DIFFERENT FLOW RATES AT ROTOR ENTRANCE.

The flow should be expected to be periodic in the circumferential direction. Figure 25 shows that the dimensionless velocity components are not exactly equal at $\theta^* = 0$ and at $\theta^* = 1$ due to experimental imprecision.

Figure 26 shows the variation of the circumferential velocity component, $V^*_{2\theta}$, along with the circumferential, θ^*, and axial, z^*, directions for $\Phi = 0.050$.

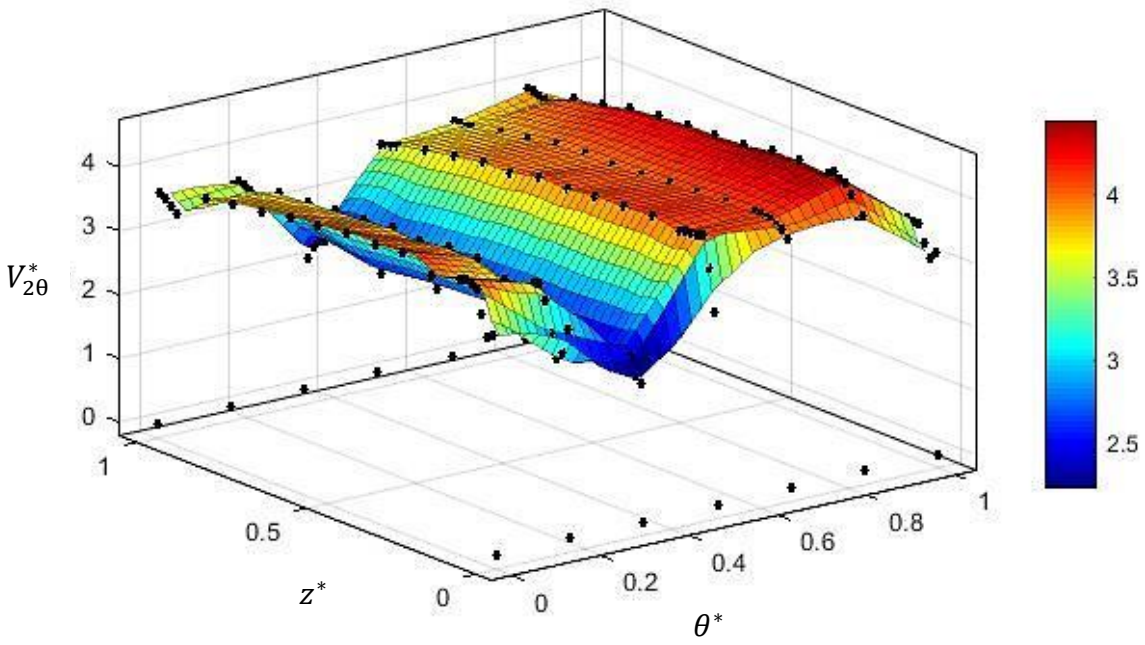

FIGURE 26. CIRCUMFERENTIAL VELOCITY COMPONENT ALONG THE CIRCUMFERENTIAL AND AXIAL DIRECTIONS FOR $\Phi = 0.050$.

Rotor exit traverses were performed at a distance of 66 mm of the rotor exit due to space constraints. Figure 27 shows the angle variation along the radial direction and Figure 28 presents the variation of the dimensionless velocity components along the spanwise direction, s^*. We define the angle at rotor exit, α^*_3, and the dimensionless velocity components, $V^*_{3\mathrm{m}}$ and $V^*_{3\theta}$:

$$\alpha^*_3 = \arctan\left(V^*_{3\theta} \Big/ V^*_{3\mathrm{m}}\right), \tag{3.9}$$

$$V^*_{3\mathrm{m}} = \frac{V_3 \cos\alpha_3}{\bar{V}_{3\mathrm{m}}}, \tag{3.10}$$

$$V_{3t}^{*} = \frac{V_3 \sin \alpha_3}{\bar{V}_{3m}}, \tag{3.11}$$

$$\bar{V}_{3m} = \frac{\int_{R_i}^{R_e} V_{3m}^2(r) r \, dr}{\int_{R_i}^{R_e} V_{3m} r \, dr}. \tag{3.12}$$

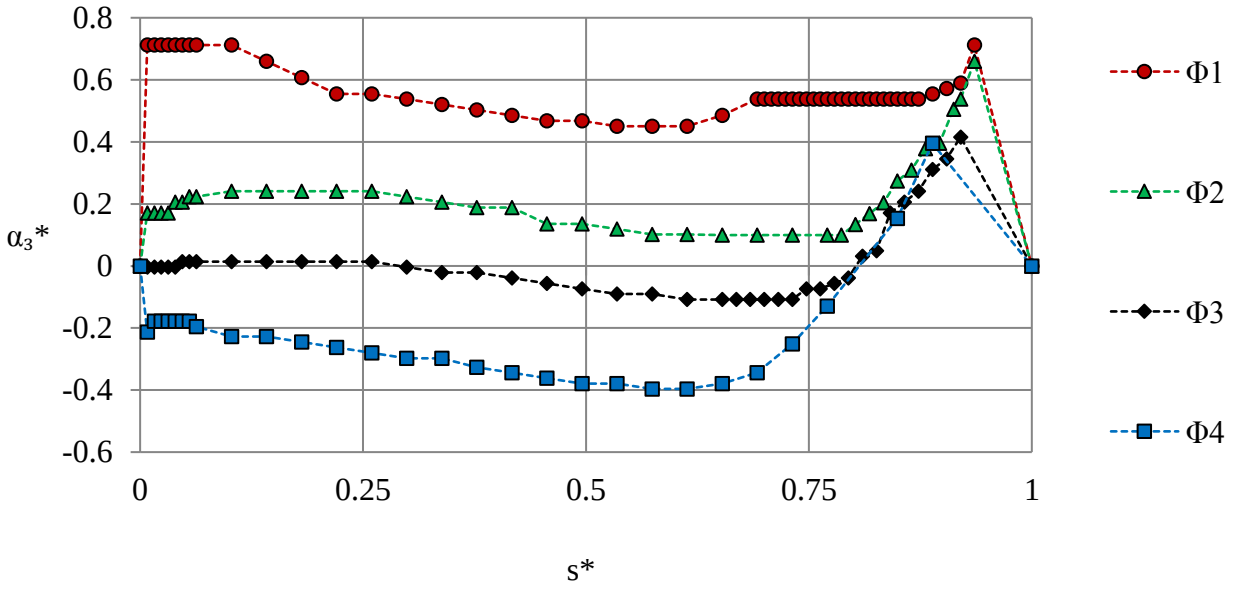

FIGURE 27. DIMENSIONLESS PLOT OF THE VELOCITY ANGLE ALONG THE SPANWISE DIRECTION AT ROTOR EXIT.

As expected, the angle can be positive or negative, depending on the flow rate coefficient, i.e. depending on the signal of the circumferential component of the velocity at rotor exit. At $s^* \approx 1$ we may see the influence of the hole through which the three-hole probe is introduced to perform the measurements.

Figure 28 shows that the meridional component of the velocity is always positive. The circumferential component can be positive or negative as anticipated before.

We should expect to have the minimum swirl at the flow rate coefficient, between Φ_2 and Φ_3, for which the efficiency is maximum. Not unexpectedly, even under peak efficiency conditions, the circumferential velocity component was found not to be exactly zero, which can be

explained by the rotor blading geometrical design and also by the limited precision of the measurements.

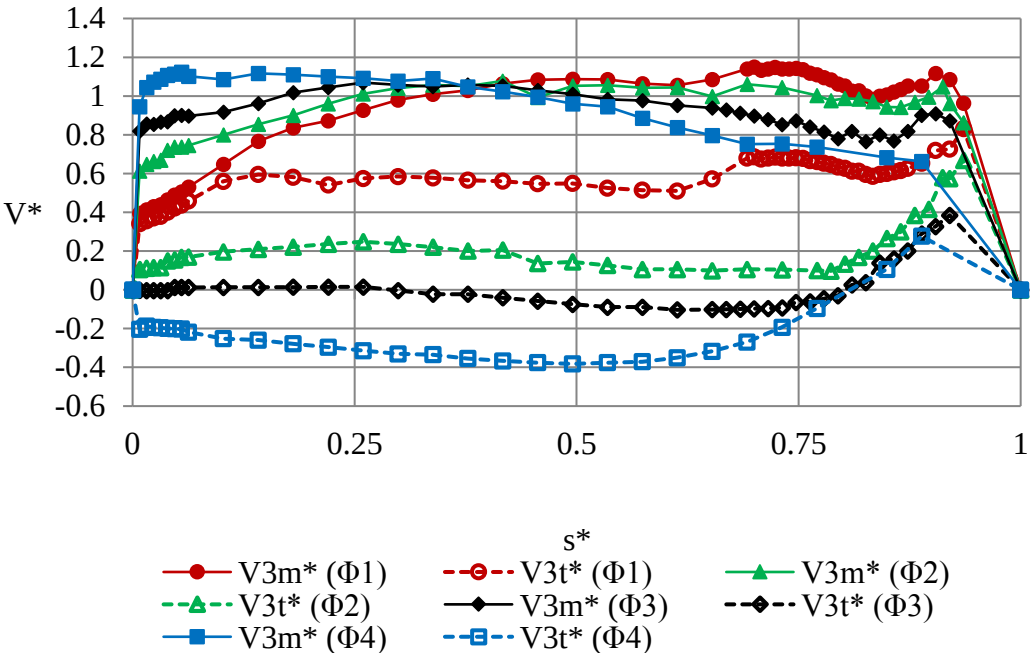

FIGURE 28. DIMENSIONLESS VELOCITY COMPONENTS ALONG THE SPANWISE DIRECTION FOR DIFFERENT FLOW RATES AT ROTOR EXIT.

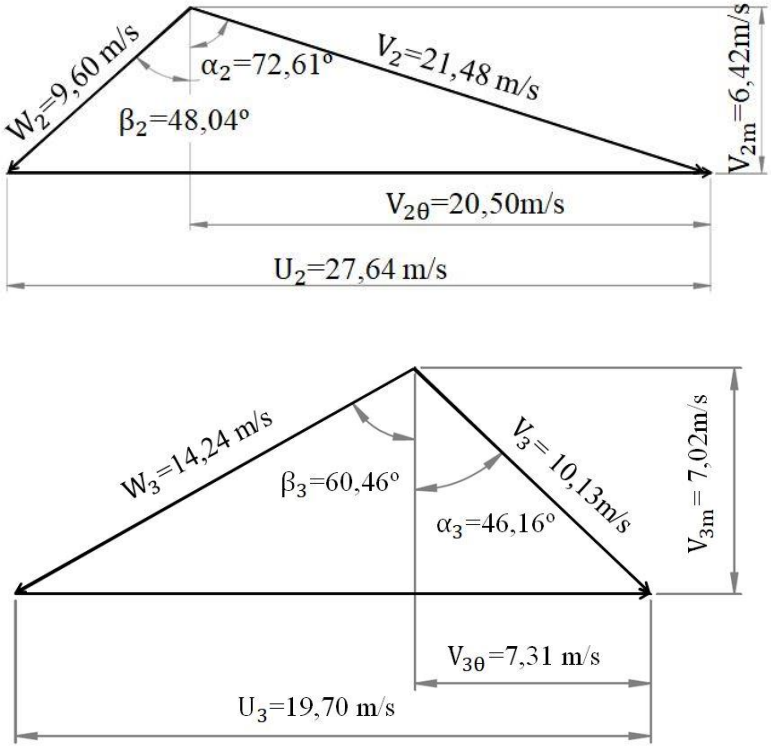

FIGURE 29. VELOCITY DIAGRAM AT ENTRY TO (SUBSCRIPT 2), AND EXIT FROM (SUBSCRIPT 3), THE ROTOR BLADES FOR $\Phi = 0.040$.

The velocity diagrams at the entry to (subscript 2), and exit from (subscript 3) the rotor blades are plotted in Figure 29 for $\Phi = 0.040$. Vector U is blade tip velocity ($U = \Omega D_{\text{tip}}/2$), and vectors V and W are absolute and relative flow velocities, respectively. It is $U_2 \neq U_3$ because the velocity diagrams correspond to different radii. As the passage area is different at the entry to, and exit from, the rotor blades, it is $V_{2\text{m}} \neq V_{3\text{m}}$.

From the Euler turbomachinery equation, we can determine the work done per unit mass:

$$E_r = U_2 V_{2\theta} - U_3 V_{3\theta}. \qquad (3.13)$$

Figure 30 shows the variation of the measured work done per unit mass with the volumetric flow rate. As expected, E_r increases with Φ.

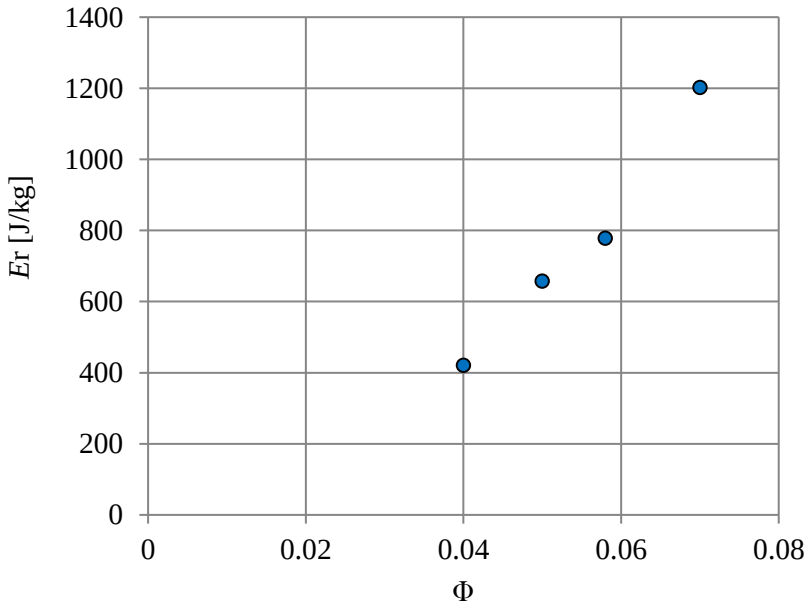

FIGURE 30. WORK DONE PER UNIT MASS, MEASURED VALUES.

3.3. Diffuser traverses

Due to space constraints, no pressure and velocity measurements could be done at the entrance to the curved-duct manifold, at radius $R_4 = 375$ mm. Instead, such measurements were performed at radius $R_{4*} = 884$ mm (see Figure 12) using a calibrated three-hole pressure probe. These measured results are identified by subscript 4. Traverses were performed along the axial direction between walls ($z^* = 0$ is the inlet wall and $z^* = 1$ is the outlet wall, where a hole is located to allow the introduction of the probe for the measurements).

The angle of the velocity vector with the radial direction, at radius R_{4*}, is defined as $\gamma = \arccos(V_{4r}/V_4)$. Its variation with the axial direction is presented in Figure 31. The studied dimensionless flow rate coefficients are the same as at rotor's entrance traverses. As expected, Figure 31 shows that the flow angle, γ, can be positive or negative, depending on the flow rate coefficient; the signal of the angle is dependent on the signal of the circumferential component of the velocity.

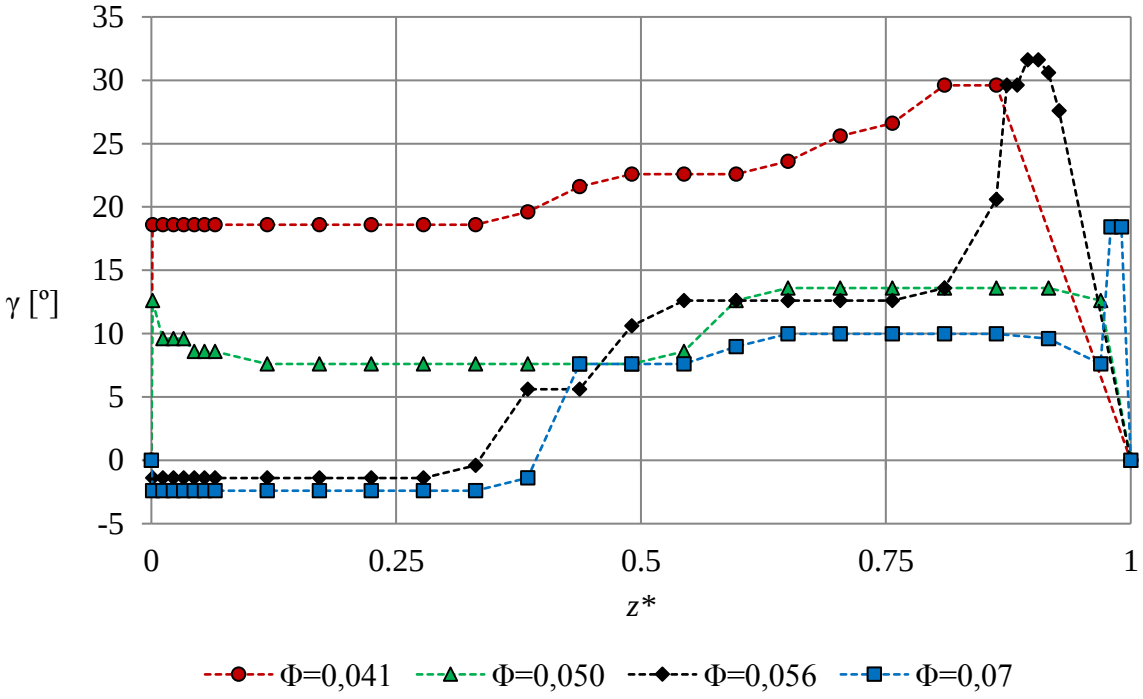

FIGURE 31. AXIAL VARIATION OF VELOCITY ANGLE γ AT RADIUS R_{4*}.

3.4. Curved-duct and manifold performance

The diffusor shaped as a curved-duct manifold is the novel part of the twin-rotor turbine. In order to analyse the capacity of the connecting duct and the diffusor to recover the kinetic energy at rotor exit, we define the recovery coefficient ε_0:

$$\varepsilon_0 = \frac{2(p_B - p_3)}{\rho \bar{V}_3^{\,2}}, \tag{3.14}$$

here p_B and p_3 are the static pressure at the plenum chamber and at rotor exit, respectively. $\bar{V}_3$ is the average velocity at rotor exit determined by the ratio of volumetric flow rate and rotor exit section area.

As seen in Figure 32 the recovery coefficient reaches its maximum (0.914) at $\varepsilon_0 = 0.05$. For a range $0.041 < \Phi < 0.075$, the coefficient exceeds 0.6, which means that in the indicated range, the connecting duct and the diffusor are recovering more than 60% of the kinetic energy associated with the axial flow velocity component at rotor exit. Naturally, if ε_0 were larger than unity, the recovered energy would also have to include part of the swirl velocity, associated to the circumferential component of the velocity.

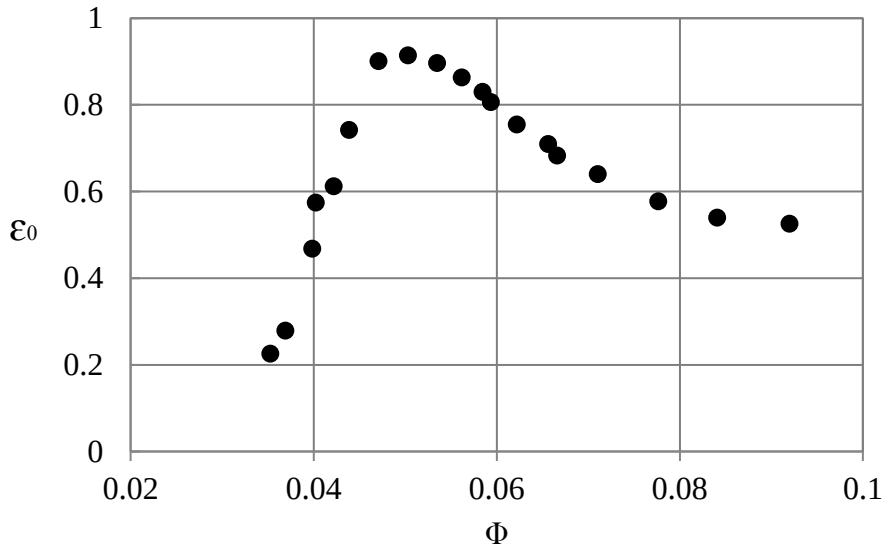

FIGURE 32. RECOVERY COEFFICIENT ε_0 VERSUS DIMENSIONLESS FLOW COEFFICIENT.

3.5. Turbine losses

It is important to evaluate the losses along the turbine. The loss coefficient is defined as

$$\Lambda = p_{\text{loss}}/\Delta p, \tag{3.15}$$

where p_{loss} is pressure loss in units of pressure and Δp is the pressure head across the turbine. The losses between the atmosphere and rotor entrance are represented by Λ_1; Λ_2 refers to rotor losses; Λ_3 accounts for losses between rotor exit and plenum chamber. It should be $\eta + \sum_{i=1}^{3} \Lambda_i = 1$.

Figure 33 shows the losses for different flow rates. Λ_1 are nearly constant. As expected, rotor losses, Λ_2, are the most significant ones.

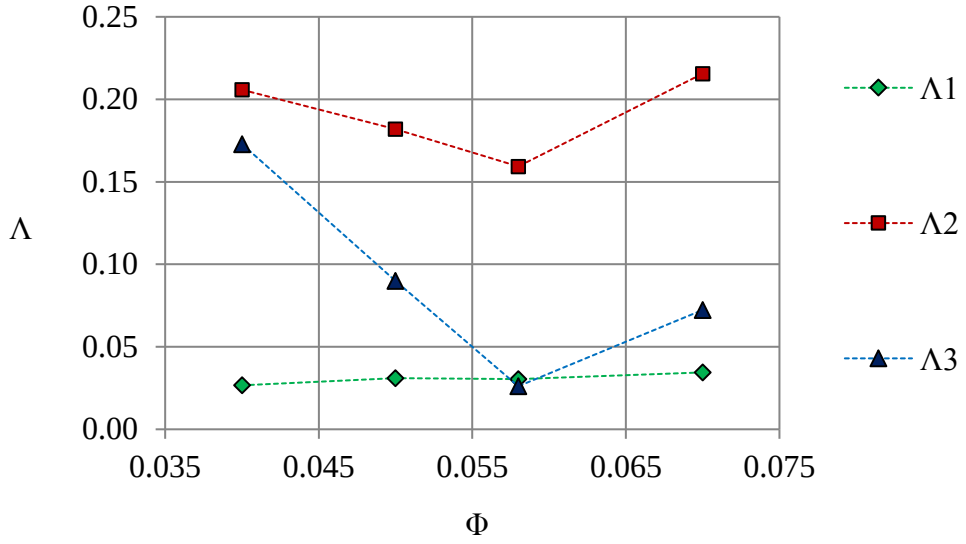

FIGURE 33. DIMENSIONLESS PLOT OF LOSSES Λ VERSUS FLOW RATE.

3.6. Efficiency curves

It is important to distinguish two cases: the simple and the twin-rotor turbine, Figure 34.

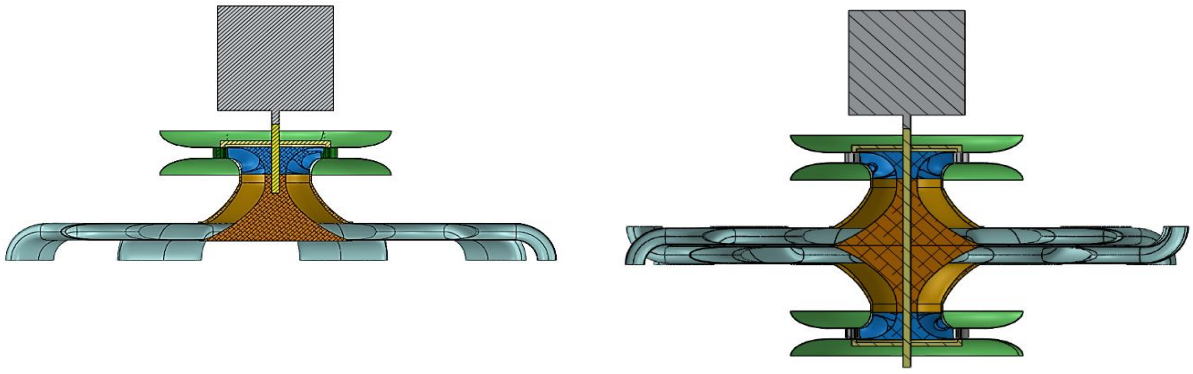

(A) **(B)**

FIGURE 34. A) SIMPLE TURBINE. B) TWIN-ROTOR TURBINE.

The simple turbine (Figure 34 a)) includes one rotor and corresponding guide vanes, one connecting duct and one diffuser, whereas the twin-rotor turbine (Figure 34 b)) is composed of two rotors and respective guide vanes, two connecting ducts and two diffusers. In the twin-

rotor turbine, we have to account for the losses in the passive rotor that were discussed previously in section 3.1.

Figure 35-37 show the turbine power output and the pressure head versus volumetric flow rate, respectively. The rotational speeds of the plotted results are between 74 and 137 rad/s. Both coefficients increase with flow rate. In contrast to axial-flow turbines (Wells or impulse), the pressure coefficient is non-zero at zero flow rate coefficient, as is usual in radial-flow rotors.

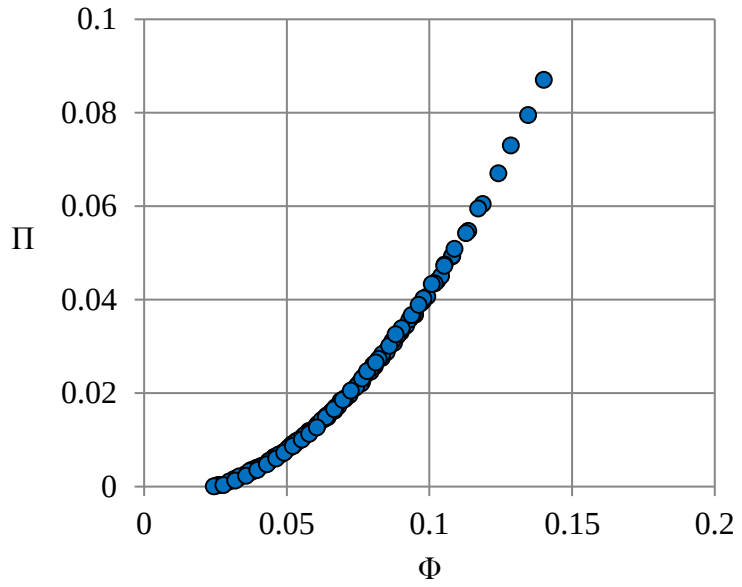

FIGURE 35. SIMPLE TURBINE POWER OUTPUT VERSUS VOLUMETRIC FLOW RATE.

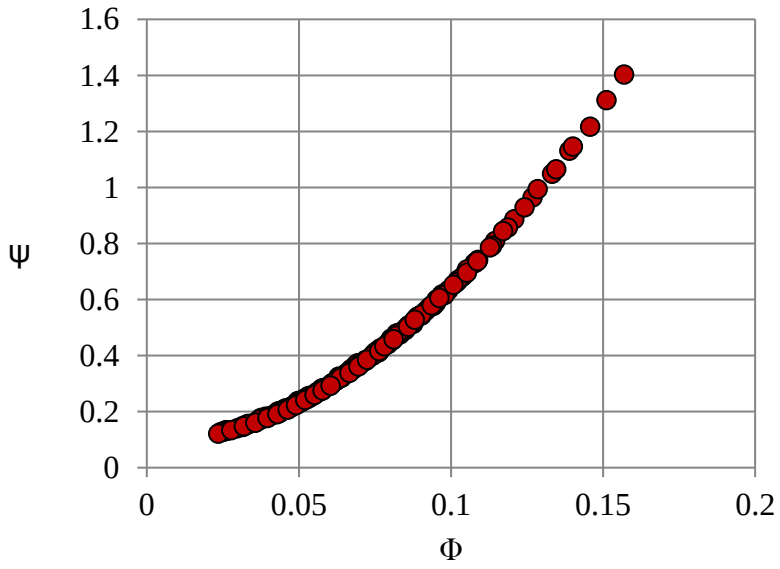

FIGURE 36. SIMPLE TURBINE PRESSURE HEAD VERSUS VOLUMETRIC FLOW RATE.

The total-to-static efficiency of the simple turbine is plotted in Figure 37.

The maximum efficiency measured experimentally is 86.6% for $\Phi = 0.05$ and it is observed that for $0.035 < \Phi < 0.070$ the efficiency is higher than 80%.

The uncertainty of the measurements (Holman, 2001) is also represented in Figure 37. As expected, the uncertainty decreases with the increase in flow rate.

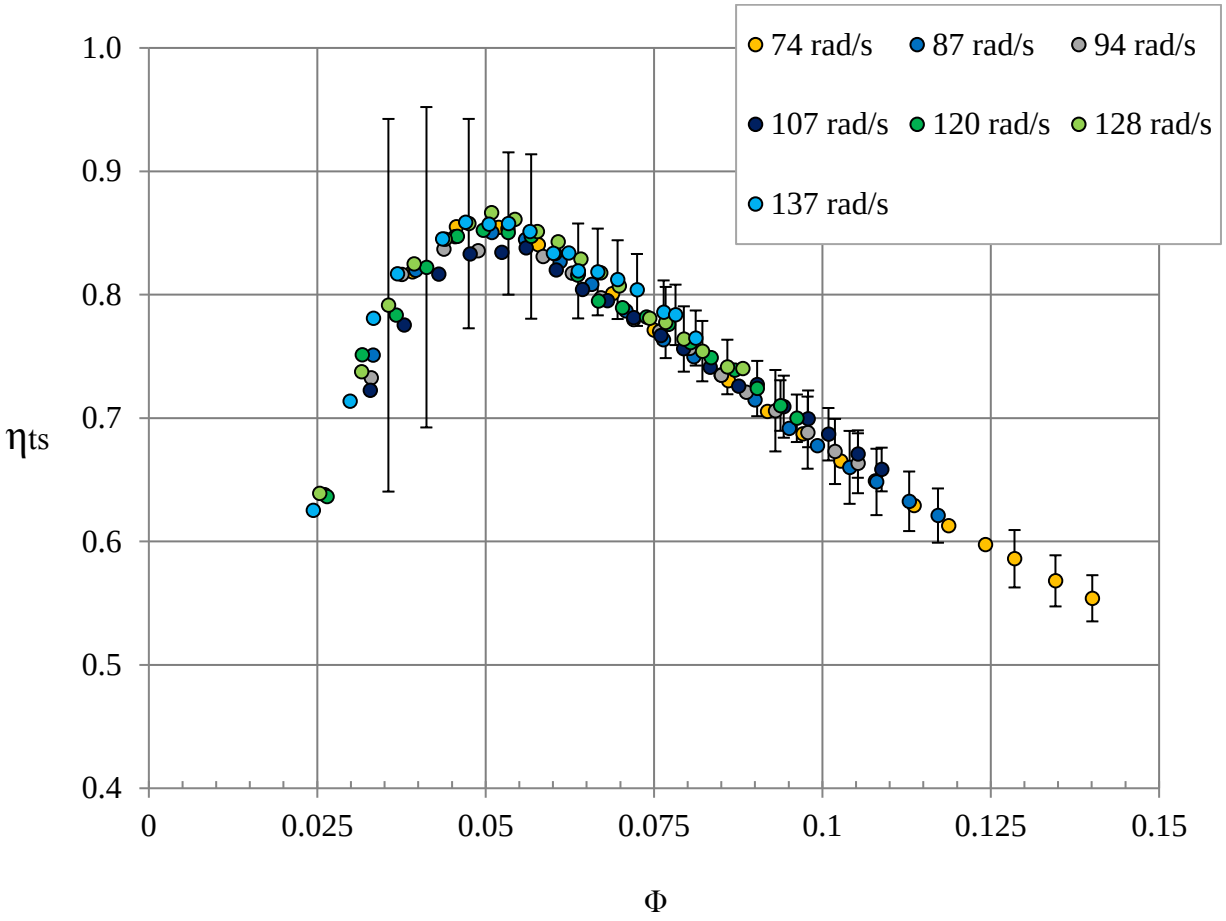

FIGURE 37. SIMPLE TURBINE EFFICIENCY VERSUS VOLUMETRIC FLOW RATE.

Accounting for the losses in the passive rotor we define the twin-rotor turbine power output as $\Pi_{\text{net}} = \Pi_{\text{simple turbine}} - \Pi_{\text{windage losses}}$. The windage losses power coefficient is $\Pi_{\text{windage losses}} = b/(\rho D^5)$, b was determined in section 3.1.

Figure 38 presents, in the dimensionless form, twin-rotor turbine power output versus flow rate.

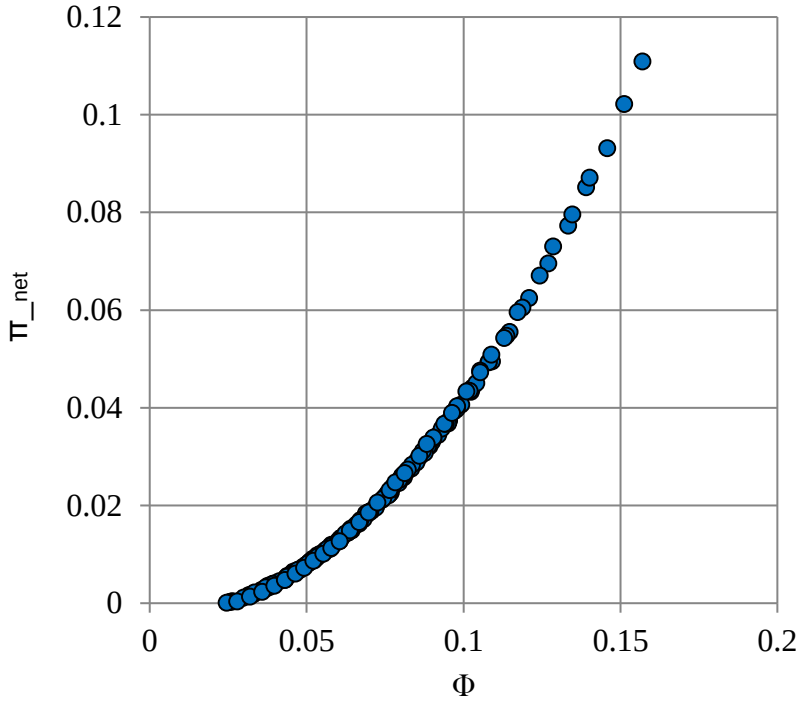

FIGURE 38. DIMENSIONLESS TWIN-ROTOR TURBINE POWER OUTPUT VERSUS FLOW RATE.

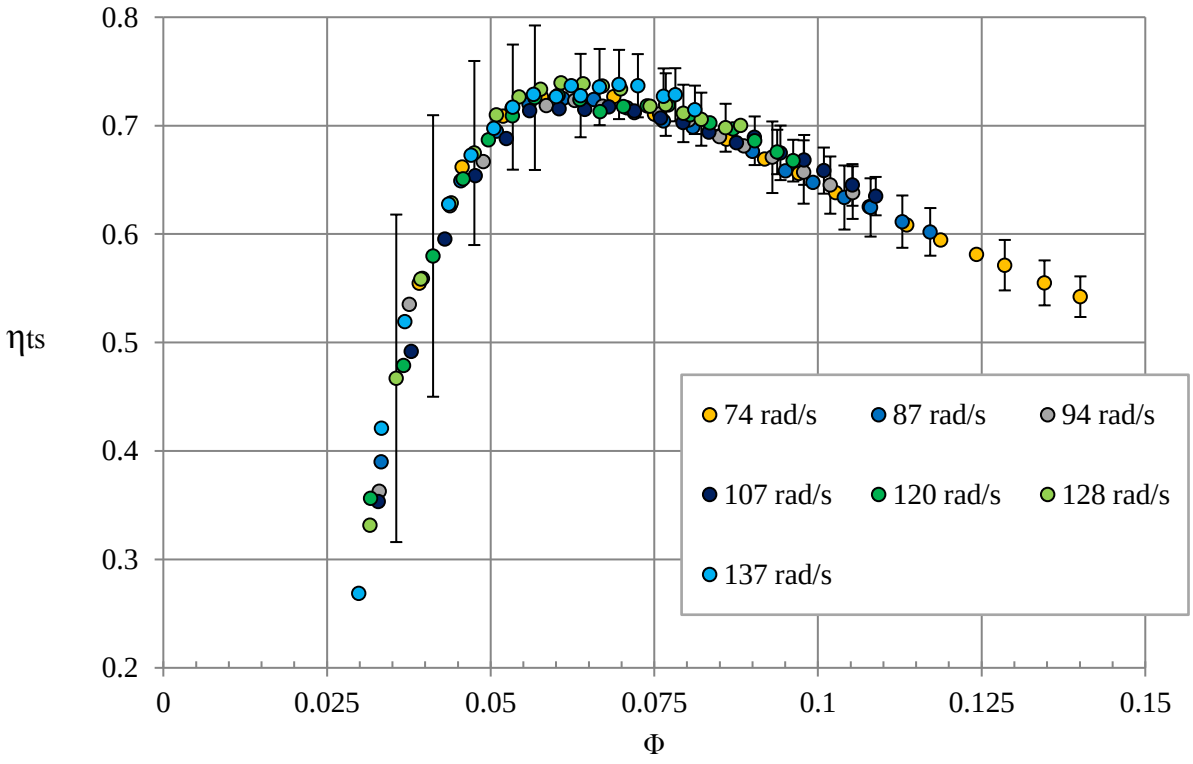

FIGURE 39. TWIN-ROTOR TURBINE EFFICIENCY VERSUS VOLUMETRIC FLOW RATE.

In both cases (simple turbine and twin-rotor turbine) the pressure head is the same because the pressure head is evaluated between the atmosphere and the plenum chamber (see Eq. 3.1). Due to that, the twin-rotor turbine pressure head versus flow rate is also represented by Figure 36.

Figure 39 presents the twin-rotor turbine efficiency. The maximum efficiency measured experimentally is 73.9% for $\Phi = 0.06$. Due to the passive rotor and its windage loss, the peak efficiency decreased by almost 12% relative to the single turbine, i.e. half of the turbine, without the passive rotor. As before, the uncertainty of the measurements is also represented in Figure 39 and it decreases with the increase in flow rate.

3.7. Performance in irregular waves

In real irregular waves, the twin-rotor turbine will operate under random pressure head conditions. Therefore, it is important to predict its average performance under such conditions.

A stochastic model was used to evaluate the twin-rotor turbine performance under irregular sea wave conditions. It is assumed in the stochastic model that (i) waves are Gaussian processes and they are represented by a spectral distribution; (ii) linear water wave theory is applicable (small amplitude waves); (iii) the system is linear (Ψ/Φ=constant, constant rotational speed in a given sea state).

As seen before, the turbine is nonlinear. However, the use of stochastic modelling for non-linear systems is much more difficult and is out of the scope of this work. For this reason, the presented results should be seen as an approximation. We define the averaged turbine efficiency as the ratio between the dimensionless average power output and the dimensionless average power available to the turbine, $\bar{\eta} = \overline{\Pi}/\overline{\Pi}_{\mathrm{avai}}$. The average power output is given by

$$\overline{\Pi}(\sigma_\Psi) = \frac{1}{\sqrt{2\pi}\sigma_\Psi}\int_{-\infty}^{\infty} \exp\left(-\frac{\Psi^2}{2{\sigma_\Psi}^2}\right)\Pi(\Psi)\mathrm{d}\Psi, \tag{3.16}$$

where σ_Ψ is the dimensionless standard deviation or root-mean-square of Ψ,

$$\sigma_\Psi = \frac{\sigma_\mathrm{p}}{\rho\Omega^2 D^2}, \tag{3.17}$$

and σ_p is the standard deviation of the pressure head Δp. The average available power output

is

$$\overline{\Pi}_{disp}(\sigma_\Psi) = \frac{1}{\sqrt{2\pi}\sigma_\Psi}\int_{-\infty}^{\infty} \exp\left(-\frac{\Psi^2}{2{\sigma_\Psi}^2}\right)\Phi(\Psi)\Psi d\Psi, \tag{3.18}$$

where σ_Ψ is the variance of Ψ. The curves (in dimensionless form) of Π(Ψ) (power output versus pressure head) and Φ(Ψ) (flow rate versus pressure head) were obtained from experimental results. The averaged turbine efficiency is represented in Figure 40. The efficiency curve obtained in laboratory experiments (steady flow) is represented in the same figure. The maximum averaged turbine efficiency is 59.9% for σ_Ψ=0.423. In order to achieve a maximum turbine average efficiency, the rotational speed should be controlled in such a way that σ_Ψ=0.423.

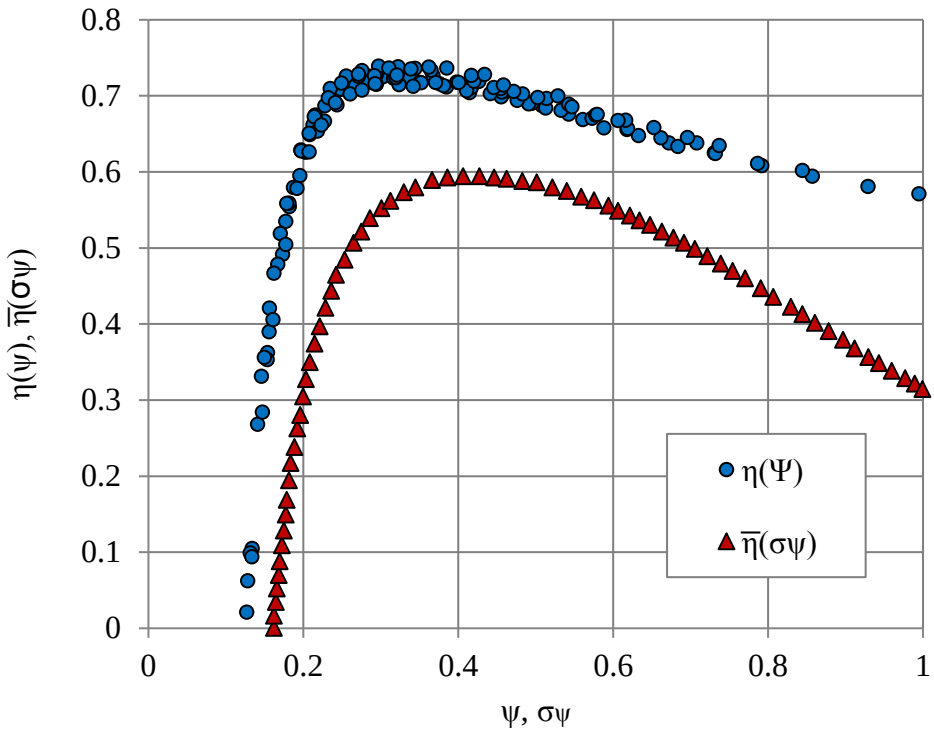

FIGURE 40. EFFICIENCY VERSUS FLOW RATE, $\eta(\Psi)$, AND AVERAGE EFFICIENCY IN IRREGULAR WAVES VERSUS RMS OF PRESSURE HEAD, $\overline{\eta}(\sigma_\Psi)$.

4. Engineering considerations

4.1. Comparison of the twin-rotor turbine efficiency with other self-rectifying turbines

It is interesting to compare the twin-rotor turbine efficiency with the efficiency of other self-rectifying turbines commonly used in OWC. The most common air turbines for wave energy conversion are the axial-flow impulse turbine and the Wells turbine. Figure 41 presents the experimental efficiency curves for the twin-rotor turbine, for a bi-plane Wells turbine with intermediate guide-vanes (see (Alves, 2013)) and for an axial-flow impulse turbine with pitching guide-vanes (see (T. Setoguchi, 2001)).

The Wells biplane efficiency curve has a sharp drop, typical of this kind of turbines. Its maximum efficiency is 62.5%. The maximum efficiency of the impulse turbine is about 60%, which is slightly below the peak efficiency of the Wells turbine. Unlike the Wells turbine, when the ratio $\Phi/\Phi_{\eta\,max}$ increase above unity, the efficiency has a smooth decrease.

The efficiency of the twin-rotor turbine exceeds the efficiency of the other two turbines. Its peak efficiency is 73.9%. Like the impulse turbine, when $\Phi/\Phi_{\eta\,max}$ increase above unity, the efficiency of the twin-rotor turbine decreases smoothly.

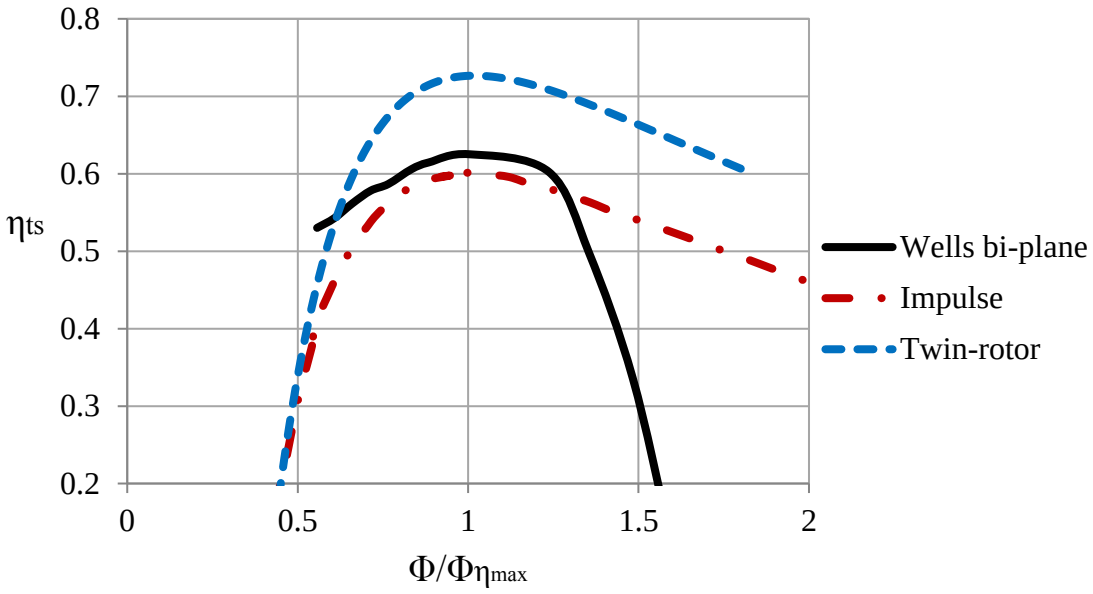

FIGURE 41. EFFICIENCY VERSUS FLOW RATE RATIO $\Phi/\Phi_{\eta\,max}$, WHERE SUBSCRIPT η_{max} MEANS MAXIMUM EFFICIENCY CONDITIONS.

The comparison between the biradial turbine and the twin-rotor turbine is also interesting. The biradial turbine has two versions: (i) with axially-sliding guide vanes and (ii) with fixed guide vanes. The efficiency curves of the second version are not published. Due to that, we will compare the twin-rotor turbine experimental performance with the first version of the biradial turbine (Nunes, 2011).

Figure 42 presents the total-to-static efficiency of both turbines. As before, the volumetric flow rate was normalized by the flow rate to maximum efficiency.

The maximum efficiency of the biradial turbine with axially-sliding guide vanes is 79% while the maximum efficiency of the twin-rotor turbine is 73.9%. The shape of the curves is very similar and the biradial turbine efficiency is a little higher than the twin-rotor. The main disadvantage of the biradial turbine with axially-sliding guide vanes is the mechanical complexity associated with the displacement of the guide vanes.

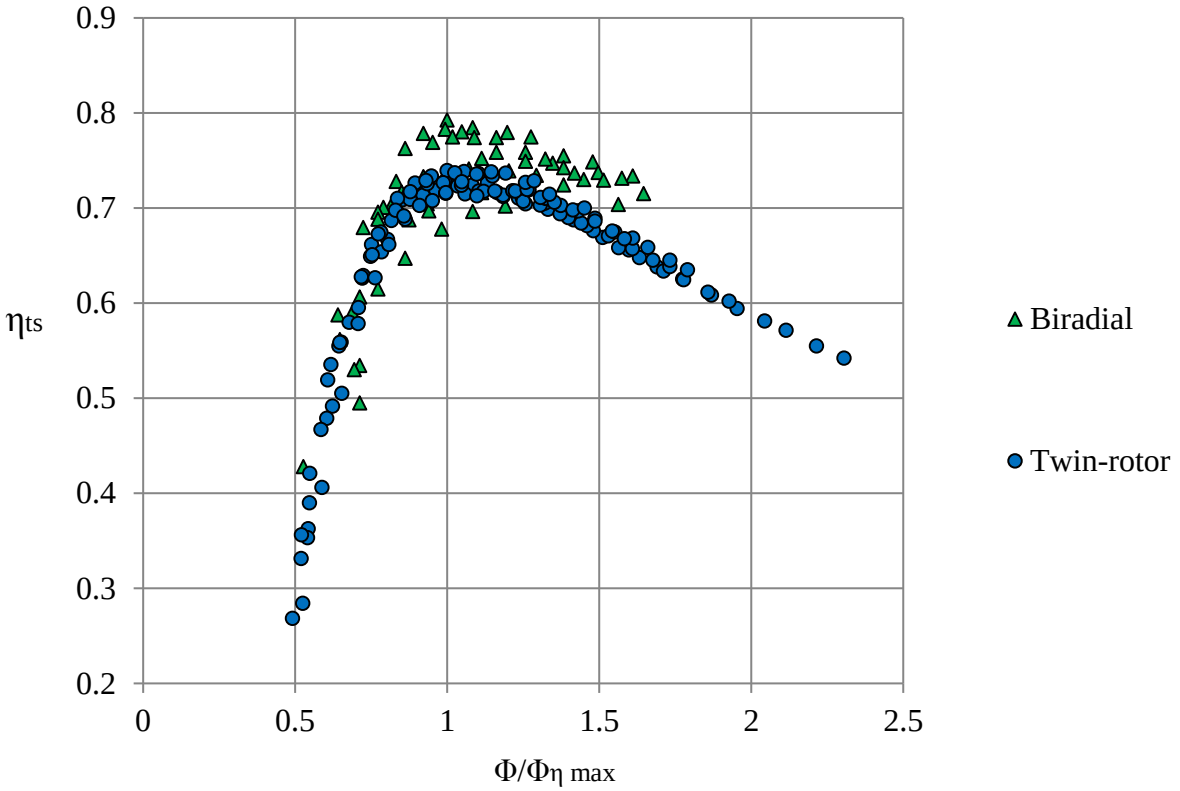

FIGURE 42. TOTAL-TO-STATIC EFFICIENCY VERSUS NORMALIZED VOLUMETRIC FLOW RATE.

4.2. New twin-rotor turbine design

The self-rectifying air turbine reported above is protect by Patent WO2014185806. A detailed engineering analysis of this turbine was performed within WP4. This turbine configuration includes a double set of large size curved ducts manifold and axisymmetric connecting ducts that were found to be expensive to manufacture. Furthermore, in the current design, the built-in axially-sliding cylindrical valve has limited access for maintenance. The engineering analysis resulted in a new design, object of a new patent submitted to the European Patent Office (Patent PT 109624 - PCT/PT2017/000016).

The new design of the twin-rotor turbine and rectification system configuration allows the device to attain the performance of conventional turbines with a rectification capability that is affordable to build and maintain.

One version of the new design is schematically shown in Figure 43, representing a section of a plane containing the rotors rotation axis. Figure 44 shows an outer view of the same implementation. The overall system operates between the first space (A) and the second space (B). These spaces are the pneumatic chamber of an OWC device and the atmosphere. The system is divided into the first sector (100) and the second sector (200), the places where conversion of pneumatic energy into mechanical energy occurs. The electrical generator (300) is located in the centre.

The system configuration has the following key characteristics: (i) inside the first sector (100) there is a ducting for unidirectional flow of the working fluid, from the second space (B) to the first space (A); (ii) in the first sector (100) there is one rotor that converts pneumatic energy into mechanical energy; (iii) inside the second sector (200) there is a ducting for unidirectional flow of the working fluid, from the first space (A) to the second space (B); (iv) in the second sector (200) there is one rotor that converts pneumatic energy into mechanical energy; (v) the ducting of the first sector (100) does not intersect the ducting of the second sector (200); (vi) the selection of the sectors through which the working fluid flows is done by the valves (170) and (270).

The valves have one or more movable components, such as cylindrical or plug obturator, which depending on the position, block or allow fluid flow in the sector ducts.

Considering the case where the pressure in the second space (B) is larger than the pressure in the first space (A), $p_B > p_A$, as in the representation of Figure 43 -(i), the second valve (270) is in the "closed" state and the first valve (170) is in the "open" state. Therefore, the working fluid flows from the second space (B) to the first space (A). It flows in the route of the first sector (100) and energy conversion occurs in the first rotor (110).

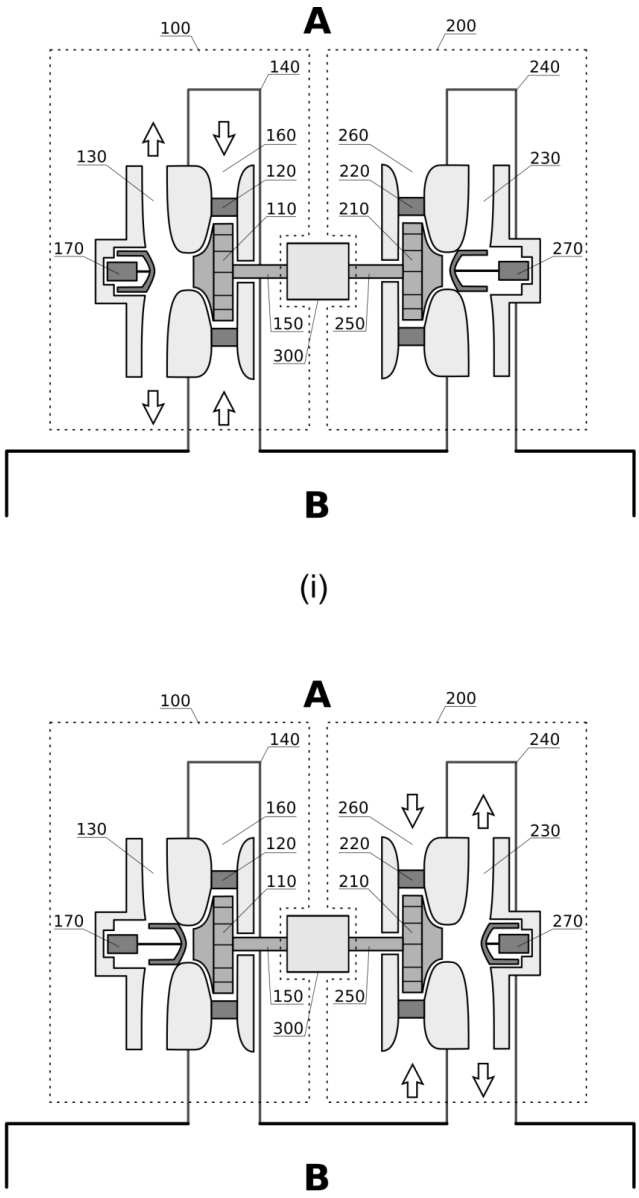

FIGURE 43. SCHEMATIC REPRESENTATION OF A CROSS-SECTION OF THE NEW TWIN-ROTOR TURBINE DESIGN BY A SYMMETRY PLANE THAT CONTAINS THE AXIS OF ROTATION OF ITS ROTORS.

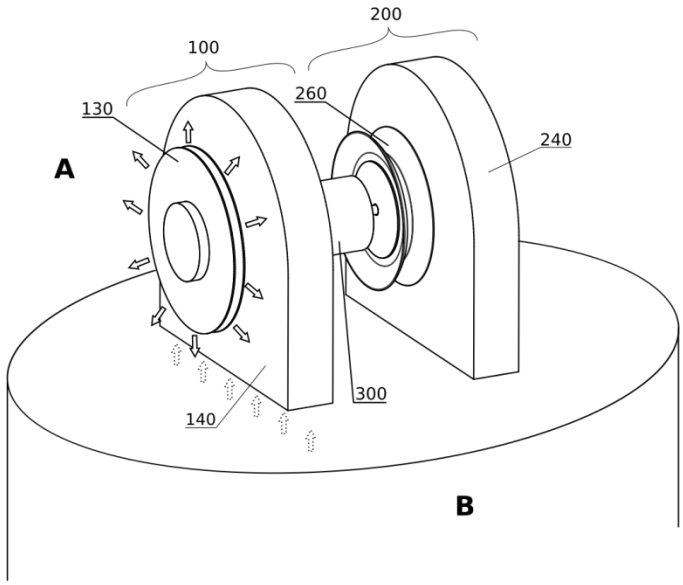

(i)

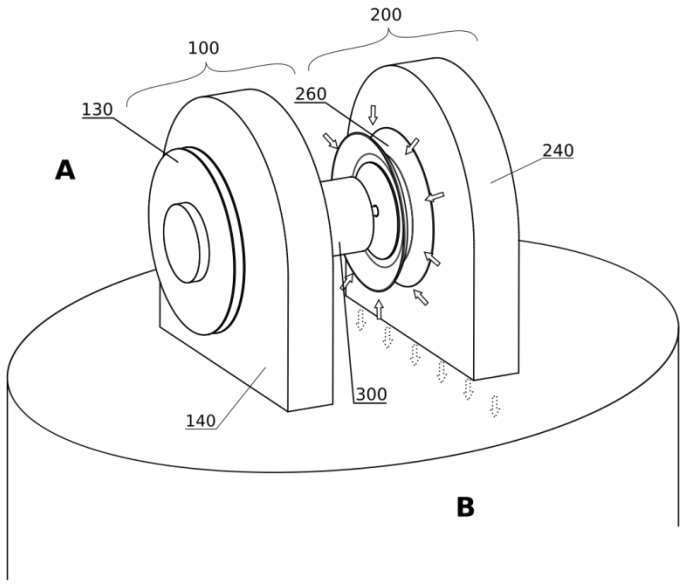

(ii)

FIGURE 44. PERSPECTIVE OF THE NEW TWIN-ROTOR TURBINE IN THE SAME CONFIGURATION AS THE REPRESENTATION OF FIGURE 43.

When $p_A > p_B$, as represented in Figure 43 -(ii), the first valve (170) is in the "closed" state and the valve (270) is in the "open" state. Therefore, the working fluid flows from the first space (A) to the second space (B), passing by the ducting of the second sector (200), with energy conversion on the second rotor (210).

The first valve (170) and the second valve (270) can actuate simultaneously, blocking both routes between the first space (A) and the second space (B). This action is essential for phase control of a wave energy converter and allows a significant increase in energy extraction. A simultaneous blockage also protects the system from the exterior in case of too energetic sea states associated with extreme weather conditions. Partial blockage of the routes is a possible action to control the flow rate through the rotors. The actuation mechanism can be electrical, hydraulic, pneumatic or of another type.

The connection between any of the spaces, first space (A) or second space (B), can be achieved with a set of manifolds. These can be classified according to their function: intake manifolds or exhaust manifolds.

The application of intake and exhaust manifolds depend on the nature of the first space (A) and the second space (B). These may be confined spaces, such as a pneumatic chamber of an OWC wave energy converter, or non-confined spaces, such as the atmosphere.

In Figure 43-45, the confined space is the second space (B). In this case, the connection between the second space (B) and the first sector (100) is made by the first intake manifold (140), that collects working fluid for conversion in the first rotor (100) (Figure 43-44 (i)). The connection between the second sector (200) and the second space (B) is made by the first exhaust manifold (240) that exhaust the working fluid after conversion in the second rotor (210) (Figure 43-45 (i)).

Considering a non-confined space, such as the atmosphere, represented by the first space (A) in Figure 43-45, this space, by definition, surrounds the components of both the first sector (100) and the second sector (200). As such, the first exit duct (130) and the second exit duct (260) are in direct connection with the first space (A), making the use of manifolds optional.

The manifolds can be similar to plenum chambers or to spiral casings. For both types, the connection to the sector routes is preferably made in a direction that is perpendicular to the rotation axis of the rotors as shown in Figure 44-47.

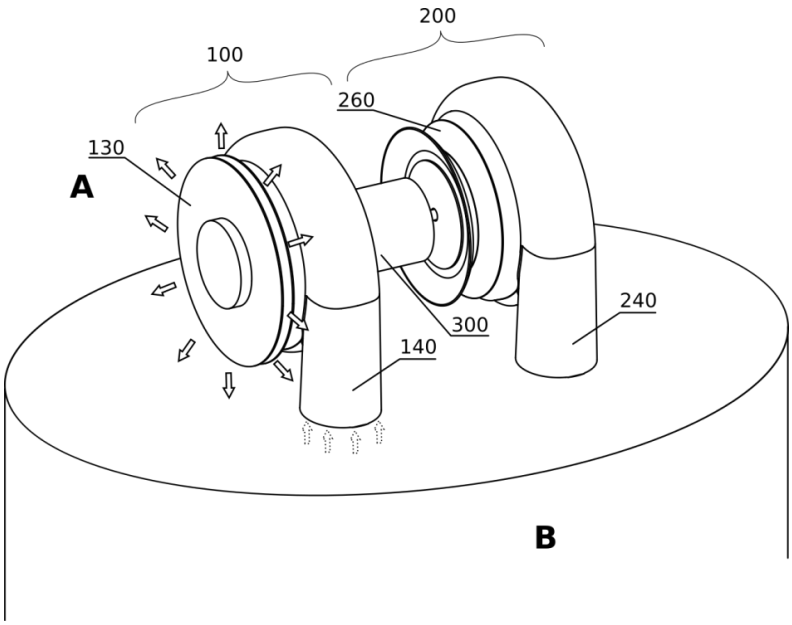

FIGURE 45. PERSPECTIVE OF THE NEW TWIN-ROTOR TURBINE WITH SPIRAL CASING NOZZLE/DIFFUSER.

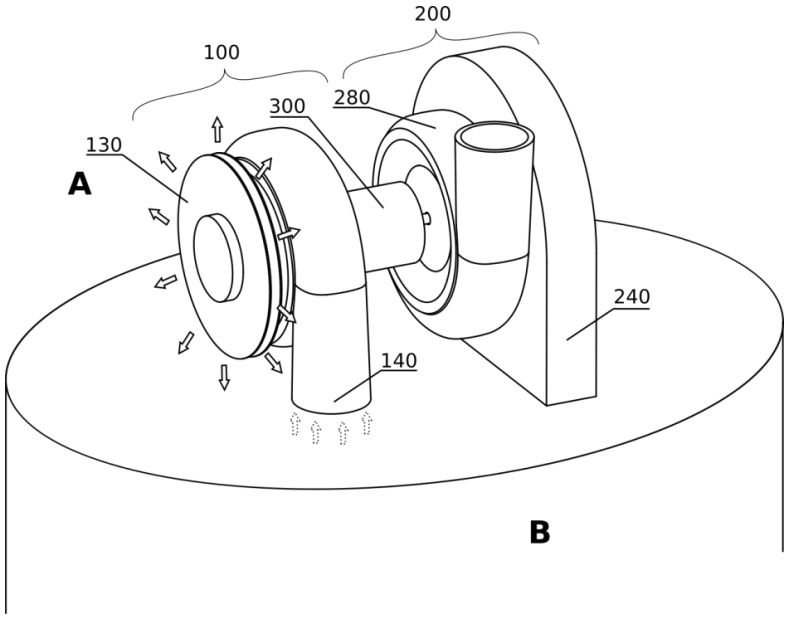

FIGURE 46. PERSPECTIVE OF THE NEW TWIN-ROTOR TURBINE WITH SPIRAL CASING NOZZLE/DIFFUSER AND PLENUM CHAMBER.

Depending on the type of intake manifolds, the system may incorporate the first guide vane system (120) and/or the second guide vane system (220) that contain one or more sets of blades that guide the flow, as shown in Figure 47-49.

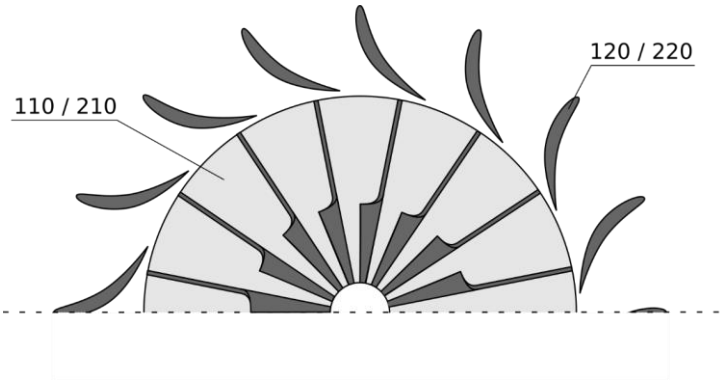

FIGURE 47 SCHEMATIC REPRESENTATION OF FIRST RADIAL-FLOW ROTOR (110), THE SECOND RADIAL-FLOW ROTOR (210), THE FIST GUIDE VANE SYSTEM (120) AND THE SECOND GUIDE VANE SYSTEM (220).

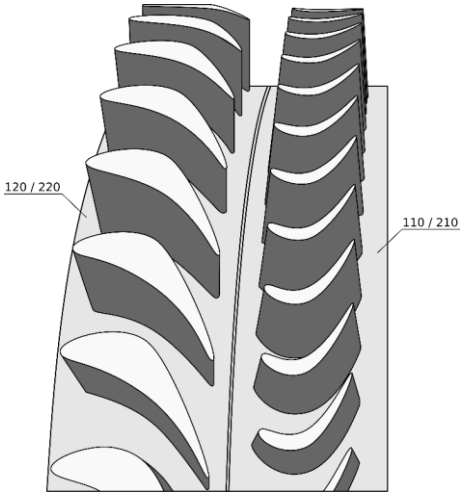

FIGURE 48 SCHEMATIC REPRESENTATION OF FIRST AXIAL-FLOW ROTOR (110), THE SECOND AXIAL-FLOW ROTOR (210), THE FIST GUIDE VANE SYSTEM (120) AND THE SECOND GUIDE VANE SYSTEM (220).

The system described here has the capability to use rotors like the ones used in conventional gas turbines. The rotors and guide vane systems can be radial (Figure 47), axial (Figure 48) or mixed-flow types. Since the flow is unidirectional, the blades can be asymmetric and with a reaction degree different from zero (reaction turbine), splitting the pressure drop between the

rotor and the guide vane system. Other configurations may also be considered: multiple sets of rotors arranged in series and/or guide vane systems with adjustable stagger angles.

To reduce the kinetic energy flow losses at rotor exit, the turbine comprises the first exit duct (130) and the second exit duct (230). These ducts convert part of the flow kinetic energy into static pressure, increasing the device total-to-static efficiency. Duct geometry can be defined by the rotation of two generatrices with respect to the rotation axis of the rotors of each sector (first sector (100) or second sector (200)).

The new turbine design combines, in the same device, the high efficiency of conventional gas turbines and the capability to extract energy in bidirectional flows, without using complex mechanisms. Apart from the rotors, the only moving parts are the valves, which have a small displacement and, when open, do not induce pressure losses on the flow. The present turbine design also allows easy maintenance access to the generator and the valves actuators from the outer side of the system. The valves can be used for phase control, safety shutdown and flow control.

4.3. Further work

The present WETFEET project is followed by the OCEANERA-NET CAPTOW project (2017-2019) which includes the design, the manufacture, and the dry testing of one 18 kW twin-rotor turbine prototype, with the new patented design, Figure 49.

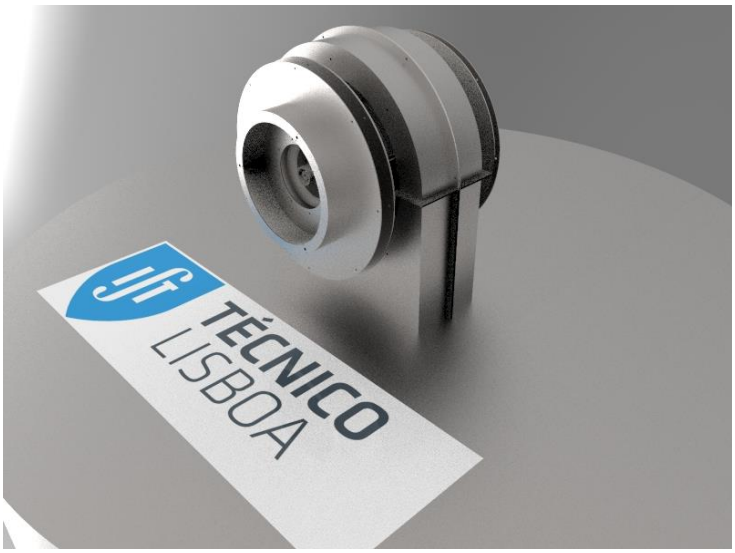

FIGURE 49. ASSEMBLY OF THE NEW PATENTED DESIGN OF THE TWIN-ROTOR TURBINE ON A FLOATING WAVE ENERGY CONVERTER.

FIGURE 50. ASSEMBLY OF THE NEW 18 KW TWIN-ROTOR TURBINE AT THE IDMEC-IST 55KW VARIABLE FLOW TURBINE TEST RIG.

The turbine prototype is currently under construction and will be tested at the IDMEC-IST 55 kW Variable Flow Turbine Test Rig, in June and July 2018, Figure 50.

An application to the MARINET 2 network program was submitted to perform field tests of the turbine at Mutriku shoreline wave power plant, with grid connection, to validate the reliability and performance of the novel twin-rotor turbine and its control algorithms.

The sea trial campaign is scheduled to start late September 2018 and will provide test data for verifying control algorithms and numerical models, accumulate experience of a real sea validation and collect the sea trial data for further performance and reliability analysis Figure 51.

Successful completion of the OCEANERA-NET and MARINET 2 projects will increase the turbine TRL from 3 to 5.

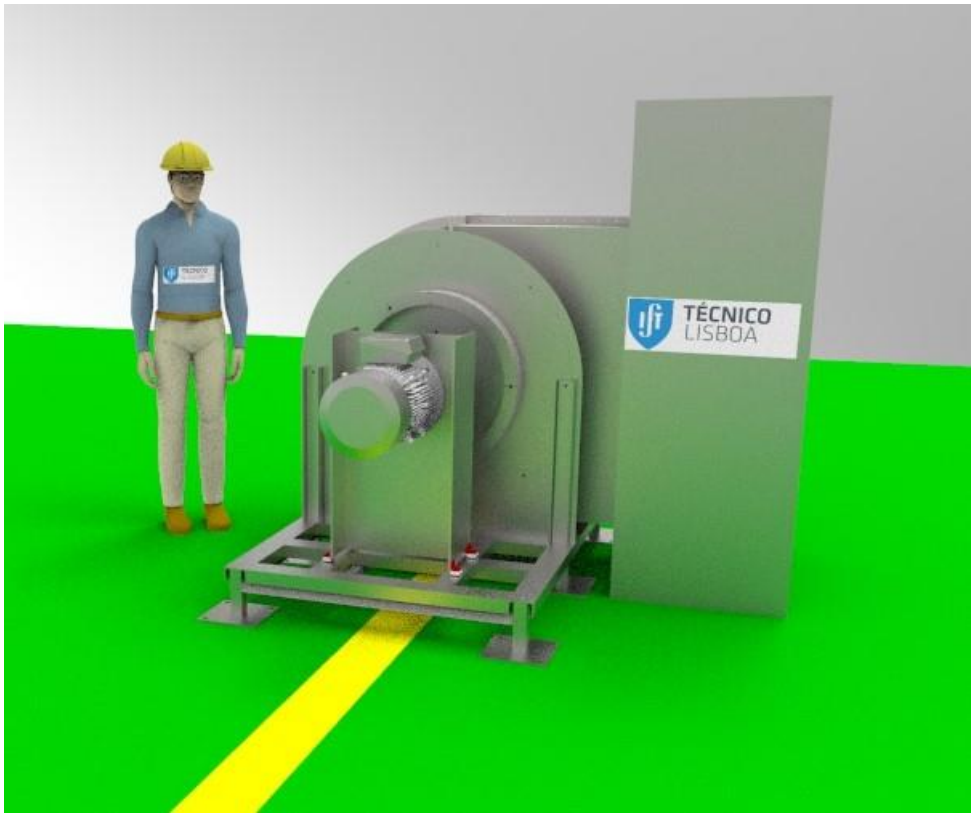

FIGURE 51. ASSEMBLY OF THE NEW 18 KW TWIN-ROTOR TURBINE AND ITS ADAPTOR FOR TESTING IN THE EXISTING MUTRIKU PLANT.

5. Conclusions

A new air turbine for bidirectional flow applications in wave energy conversion was experimentally investigated. The turbine is composed of two identical parts intertwined with each other; only half of the turbine was constructed and tested in unidirectional flow at the blow-down test rig of IST. This document presents experimental results for the single rotor (simple turbine) and for the twin-rotor turbine.

The main objective of this investigation was to study the recovered energy in the manifold diffuser, where flow velocity was found to be too small to be measured with the desired accuracy with the available equipment; this raised some problems.

The turbine flow rate was measured at the turbine entrance, where the velocity was larger, rather than at the convergent-divergent nozzle downstream of the plenum chamber as usually done in previous tests of other types of turbines in the same test rig.

The flow angle and the velocity profiles were studied in detailed traverses at rotor entrance and exit, and also at the diffuser.

The experimental results show that the curved-duct manifold and the connecting duct are able to recover most of the kinetic energy at rotor exit over a wide range of flow rates.

The plot of the turbine pressure head coefficient versus the flow rate coefficient showed that, unlike Wells turbines, the tested twin-rotor turbine is clearly a non-linear turbine at constant rotational speed.

Bearing losses were determined and added to the measured turbine power output, as is reasonable to do. Windage losses at the passive rotor were also determined and found to significantly reduce the efficiency of the twin-rotor turbine. The experimental results showed that the maximum efficiency of the twin-rotor turbine is 73.9% at a flow rate coefficient of 0.06. For the tested single-rotor turbine (without the passive rotor) the peak efficiency was found to be 86.6%. The difference, 12.7%, is due to the windage losses at the passive rotor. Windage losses are inherent to the twin-rotor turbine concept. Finding ways to reduce such losses by redesigning the rotor and/or its construction method or by using a different type of rotor (possibly of axial-flow type) are important steps to improve the competitiveness of the twin-rotor type of turbine.

Performance comparisons with other competing self-rectifying turbines show that the twin-rotor turbine clearly outperforms the biplane Wells turbine with guide vanes between planes and the axial-flow impulse turbine with pitching guide vanes.
The tested self-rectifying air turbine is protected by Patent WO2014185806. A detailed engineering analysis of this turbine was performed within WP4. This turbine configuration includes a double set of large size curved ducts manifold and axisymmetric connecting ducts that were found to be expensive to manufacture. Furthermore, in the current design, the built-in axially-sliding cylindrical valve has limited access for maintenance. The engineering analysis resulted in a new design, object of a new patent submitted to the European Patent Office Patent No. PCT/PT2017/000016, 2017.

The new design of the twin-rotor turbine and rectification system configuration allows the device to attain the performance of conventional turbines with a rectification capability that is affordable to build and maintain.

The new turbine combines, in the same device, the high efficiency of conventional gas turbines and the capability to extract energy in bidirectional flows, without using complex mechanisms. Apart from the rotors, the only moving parts are the valves, which have a small displacement and, when open, do not induce pressure losses on the flow. The present turbine design also allows easy maintenance access to the generator and the valves actuators from the outer side of the system. The valves can be used for phase control, safety shutdown and flow control.

The valves can be used for safety shutdown, flow control and to implement advanced predictive and latching control algorithms which were seen to enable large increase in power production by broaden bandwidths and increase average energy capture by more than 30%, according to model results and are seen as the most promising cost-reduction pathway for OWC (see (Henriques et al. 2016a,b)). Laboratory results for the twin-rotor turbine exhibit annual efficiency 50% higher than the Wells turbine, the currently established turbine for OWC application.

Further work is being funded by the OCEANERA-NET CAPTOW project (CAPTOW, 2017-2019) which includes the design, the manufacture, and the dry testing of one 18 kW twin-rotor turbine prototype, with the new patented design.

An application to the MARINET 2 network program (MARINET2, 2018) was submitted to perform field tests of the turbine at Mutriku shoreline wave power plant, with grid connection, to validate the reliability and performance of the novel twin-rotor turbine and its control algorithms.

References

Alves, J. S. (2013). *Experimental and CFD analysis of a biplane wells turbine for wave energy harnessing.* Master's thesis, KTH, School of Engineering Sciences.

CAPTOW. (2017-2019). *OCEANERA-NET*. http://oceaneranet.eu/portfolio/captow/

Holman, J. P. (2001). *Experimental methods for engineers.* McGraw-Hill.

Gato, L.M.C. , Ferreira, D. N., et al. (2017). *European Patent Office Patent No. PCT/PT2017/000016.*

MARINET2. (2018). http://www.marinet2.eu/

Nunes, E. P. (2011). *Turbina auto-retificadora bi-radial.* Master's thesis, Instituto Superior Técnico, Universidade Técnica de Lisboa.

Setoguchi, T. et al. (2001). A review of impulse turbines for wave energy conversion. *Renewable Energy, 23 (2)*, 261-292.

Henriques J.C.C., Gato L.M.C., Lemos, J.M., Gomes, R.P.F., Falcão, A.F.O. (2016). *Peak-power control of a grid-integrated oscillating water column wave energy converter. Energy, vol. 109, p. 378- 390, DOI: 10.1016/j.energy.2016.04.098.*

Henriques J.C.C., Gato L.M.C., Falcão, A.F.O., Robles, E., Fay, F.X. (2016). *Latching control of a floating oscillating-water-column wave energy converter. Renewable Energy, Vol. 90, pp. 229-241, DOI: 10.1016/j.renene.2015.12.065.*